TRIM67 Regulates Exocytic Mode and Neuronal Morphogenesis via SNAP47

Fabio L. Urbina[1], Shalini Menon[1], Dennis Goldfarb[2,4], M. Ben Major[2,4], Patrick Brennwald[1], Stephanie L. Gupton[1,3,4,5]

[1]UNC Department of Cell Biology and Physiology, Mason Farm Road, Chapel Hill, NC 27599, USA
[2]UNC Department of Cell Biology and Physiology, Cancer Research Building, Rm 4625
[3]UNC Neuroscience Center,Mason Farm Road, Chapel Hill, NC 27599, USA
[4]UNC Lineberger Comprehensive Cancer Center, 101 Manning Dr, Chapel Hill, NC 27514, USA
[5]Lead contact
Correspondence: sgupton@unc.edu

Abstract

Morphogenesis in developing neurons involves dramatic plasma membrane expansion, which classic hypotheses suggest is fueled by SNARE-mediated exocytosis. Distinct modes of fusion have been described; during full vesicle fusion (FVF) the entirety of vesicle contents are secreted and the vesicle membrane incorporates into the plasma membrane. In contrast, a transient fusion pore secretes lumenal cargo, but closes without membrane addition in kiss and run fusion (KNR). If exocytosis provides material for neuronal morphogenesis, this would suggest FVF predominates, although this has not been examined. Fortuitously in developing neurons, exocytic events are spatially and temporally discrete, unlike exocytic events at the neuronal synapse, allowing resolution of single vesicle fusion events although they are diffraction-limited. Here, we resolve individual exocytic events in developing murine cortical neurons, and use a newly developed classification tool to differentiate and quantify different modes of fusion. We identify four distinct modes of fusion: two FVF-like modes that insert membrane material and two KNR-like modes that do not. Within the FVF-like and KNR-like modes, discrete fluorescence profiles suggest distinct behavior of the fusion pore. Consistent with our hypothesis, FVF-like exocytosis predominates. Simulations and experimental manipulations agree that exocytosis provides sufficient amounts of membrane material for neuronal morphogenesis. Mechanistically we identify that the E3 ubiquitin ligase TRIM67 promotes FVF-like exocytosis by limiting incorporation of the Qb/Qc SNARE SNAP47 into SNARE complexes and thus, SNAP47 involvement in exocytosis. Our data suggest that SNAP47 regulates behavior of the fusion pore between the vesicle and plasma membrane, temporarily arresting the pore in an open state.

Introduction

Membrane bound compartments are a defining feature of eukaryotic cells. The transport and transfer of membrane proteins, lipids, and lumenal cargo between compartments requires membrane fusion, in which two distinct lipid bilayers merge. The opening of a fusion pore between bilayers is mediated by Soluble N-ethylamaleimide-sensitive factor Attachment protein REceptors (SNAREs). SNARE proteins assemble into a SNARE complex, the core of which is a

stable bundle of four alpha-helices (**Fig 1A)**. Specific SNAREs mediate fusion between different compartments, such as vesicle-associated membrane protein 2 (VAMP-2) and plasma membrane-associated syntaxin-1 and synaptosomal-associated protein 25 (SNAP25), which facilitate docking and fusion of synaptic vesicles at the neuronal plasma membrane (Sudhof and Rothman, 2009; Schoch, 2001; Söllner et al., 1993). Evoked exocytosis of neurotransmitters involves multiple synaptic vesicle fusion events spatio-temporally clustered at the synapse, a diffraction-limited area. This restriction renders visualization and analysis of individual fusion events difficult. During neuronal development, however, constitutive exocytosis mediated by these same SNAREs is not restricted to synapses and is sufficiently infrequent to resolve individual vesicle fusion events (Bello et al., 2016; Urbina et al., 2018).

Our previous work suggests that prior to synaptogenesis, VAMP2-mediated fusion provides significant amounts of membrane material to the expanding plasma membrane of the developing neuron, contributing to neuronal morphogenesis (Urbina et al., 2018). This developmental exocytosis becomes both spatially and temporally clustered over developmental time (Urbina et al., 2018). We found that an interaction between SNAP25 and the brain-enriched E3 ubiquitin ligase TRIM9 prevents SNARE complex formation and consequently attenuates the rate of exocytosis and axon branching in developing neurons (Winkle et al., 2014). Genetic deletion of *Trim9* also alters neuronal morphology *in vivo* (Winkle et al., 2016). Since disrupted neuronal morphology is associated with several neurological diseases (Engle, 2010; Paul et al., 2007), regulation of membrane insertion and, by extension, exocytosis, is likely critical for nervous system formation and function.

Fusion mode may be another regulatable parameter of developmental exocytosis. At the synapse, two modes of exocytosis are described, yet their contribution remains controversial (Alabi and Tsien, 2013; Albillos et al., 1997; He and Wu, 2007; Elhamdani et al., 2006). During full vesicle fusion (FVF), the fusion pore is suggested to dilate and the vesicle membrane incorporates into the plasma membrane. In contrast, during kiss and run fusion (KNR), the fusion pore opens transiently, secretes lumenal cargo, and then reseals, retaining vesicular identity (Alabi and Tsien, 2013; Albillos et al., 1997; Bowser and Khakh, 2007; Holroyd et al., 2002; Wang et al., 2003). As presumably only FVF donates membrane material, regulating the mode of exocytosis may fine tune neuronal plasma membrane expansion during development.

How the mode of exocytosis is regulated is not clear. Heterogeneous sizes of fusion pores and dilation kinetics likely vary with fusion mode. *In vitro*, the number of SNARE complexes regulate fusion pore dilation (Bao et al., 2018; Bello et al., 2016). The composition of SNARE complexes may also regulate the fusion pore. The SNARE family contains more than 60 members (Burri and Lithgow, 2004). Although VAMP2, syntaxin-1, and SNAP25 are classic neuronal exocytic SNAREs, other SNAREs form exocytic complexes. SNAP47 is an atypical SNAP25 family member that can substitute for SNAP25 in complexes with VAMP2 and syntaxin-1 *in vitro.* SNARE interacting proteins, such as synaptotagmins, complexins, α-synuclein, and TRIM9 (Archer et al., 2002; Logan et al., 2017; Wang et al., 2003; Winkle et al., 2014) are also poised to regulate the fusion pore. Similar to SNAREs, the mammalian TRIM family of ubiquitin ligases contains ~ 70 members, with many TRIMs enriched in neurons (Napolitano and Meroni, 2012). TRIM67, a paralog of the SNAP25-interacting TRIM9, is enriched in the developing cortex and regulates axonal projections, filopodia, and spatial learning and memory(Boyer et al., 2018,

2020), but thus far has not been implicated in exocytosis. The roles that TRIM67 and SNAP47 play in VAMP2-mediated fusion in developing neurons have not been explored.

Here, we use VAMP2-pHluorin expression in developing neurons to explore modes of single exocytic events. We develop computer vision classifiers to surprisingly reveal four modes of fusion. This includes two distinct classes within both FVF and KNR, which exhibit distinct fluorescence behavior following fusion pore opening. Experimental manipulations and simulations agree that membrane provided by FVF modes of VAMP2-mediated exocytosis well approximate the plasma membrane expansion of developing neurons. We show that the E3 ubiquitin ligase TRIM67 regulates exocytic mode without changing exocytic frequency. Mechanistically TRIM67 alters exocytic mode by reducing SNAP47 protein and limiting SNAP47 incorporation into SNARE complexes. We show that SNAP47 co-localizes with a subset of VAMP2-mediated exocytic events, and alters fusion mode. Our data are consistent with a model in which SNAP47 temporarily arrests the fusion pore in an open state.

Results

Heterogeneity in single vesicle fusion event kinetics

To explore the kinetics of single exocytic events, we used total internal reflection fluorescence (TIRF) microscopy to image VAMP2-pHluorin in developing murine cortical neurons. pHluorin is a pH sensitive variant of GFP that is quenched at acidic pH, such as within the vesicular lumen, but fluoresces upon fusion (Miesenböck et al., 1998)(**Fig 1A**). We identified bona fide exocytic events in a high-throughput manner using our established automated detection methods (**Fig 1B**, (Urbina et al., 2018)). To evaluate the population of fusion events, we examined the normalized peak change in fluorescence per event (peak $\Delta F/F$, **Fig 1B, 1C**), which estimates the relative amount of VAMP2-pHluorin per vesicle, and the event half-life ($t_{1/2}$, **Fig 1B, 1C'**), which describes fluorescence decay after fusion pore opening (peak $\Delta F/F$, **see methods**). Unlike the peak $\Delta F/F$, half-life exhibited a bimodal distribution, suggesting two populations of fusion events. Two classes of exocytosis are described in literature, full-vesicle fusion (FVF) and kiss-and-run fusion (KNR, **Fig 1A**)(Alabi and Tsien, 2013; Holroyd et al., 2002; Wang et al., 2003). FVF exhibits characteristic diffusion of VAMP2-pHluorin within the plasma membrane away from the fusion site (Bowser and Khakh, 2007). Without diffusion of the v-SNARE, KNR events should remain a fluorescent foci until fusion pore closure and re-acidification. To determine if the bimodal peaks of the fluorescence half-life potentially represented distinct fusion modes, we quantified peak $\Delta F/F$ in pixels surrounding exocytic events immediately after peak $\Delta F/F$ (**Fig 1D**). Categorizing events based on border pixel fluorescence aligned with the bimodality of half-life distribution (**Fig 1E**). Thus, there is sufficient information within individual VAMP2-pHluorin fusion events to differentiate populations.

Vesicles that fuse by KNR retain their identity after fusion; however, re-acidification prevents visualization of VAMP2-pHluorin. To permit visualization of vesicles before, during, and after fusion, we imaged neurons simultaneously expressing VAMP2-pHluorin and VAMP2-tagRFP (**Fig 1F**). Exponential decay of both VAMP2-pHluorin and VAMP2-tagRFP confirms diffusion of v-SNAREs during putative FVF events (**Fig 1F', top, blue**). Events without VAMP2-pHluorin diffusion maintained detectable VAMP2-tagRFP fluorescence after fusion that did not fit an exponential decay (**Fig 1F', bottom, orange**), indicating vesicles persist following putative KNR

events. Thus VAMP2-tagRFP fluorescence behavior agreed with pHluorin-based classification (**Fig 1G**), suggesting that FVF and KNR are discernable in the pHluorin-based assay.

Multiple unbiased classifiers converge on four exocytic modes

To rigorously explore the heterogeneity of fusion, we developed an unbiased classification pipeline. We captured information within ROI around each event starting two seconds prior and ending 10 seconds post peak ΔF/F; this empirically determined time-frame ensured fluorescence returned to baseline (Urbina et al., 2018). Events were then temporally registered by aligning to peak ΔF/F (**Fig 2A**). We then employed a three-pronged approach to create an unbiased classifier for vesicle fusion.

As a ground truth method, we selected features that possibly discern known differences between KNR and FVF, as well as their biological interpretation. This includes ΔF/F and the half-life of VAMP2-pHluorin fluorescence, among other parameters (**Fig 2B, see methods**). Principal Component Analysis (PCA) was performed on all features and the five principal components (PC) capturing 85% of the variance were kept (**Fig 2B'**).

The second classification utilized both agglomerative and divisive hierarchical cluster analysis **(Fig 2C)**. Agglomerative clustering summates a Euclidean distance cost (∑) between each pair of events starting at peak ΔF/F (**Fig 2Ci**), and then merges the lowest-cost events iteratively based on a linking rule until eventually all events are linked, creating a cluster dendrogram (**Fig 2Cii,** see methods). Divisive clustering first clusters all events together into one class, then iteratively divides events into smaller groups until all exocytic events have been split. Euclidean distance matrices are constructed to visualize the relationship and groupings of these events (**Fig 2Ciii**).

Finally, we utilized Dynamic Time Warping (DTW, **Fig 2D**) to measure spatio-temporal dissimilarity between a pair of ΔF/F curves. DTW allows non-linear temporal matching between events **(Fig 2Di)** to find the optimal path of smallest distance. DTW creates a time warp matrix where each square is the Euclidean distance between respective timepoints of two ΔF/F time series (**Fig 2Dii**). The optimal warp path for a pair of exocytic events is the lowest cost path through the matrix, which may be distinct from the ∑ Euclidean distance (**Fig 2Dii**). The sum of the warp path, or the dynamic time warping cost, is plotted on a distance matrix, with each pixel of the distance matrix representing the sum of the warp path for a pair of exocytic events (**Fig 2Diii**).

To computationally explore the number of exocytic classes or clusters revealed by these three methods, we took the plurality rules decision from a committee of the most common clustering indices that performed best in simulation studies (Charrad et al., 2014). This method converges on a number of clusters k, present in the data with meaningful confidence. Among the indices used were the gap statistic, which measures within-cluster dispersion, and the elbow method, which examines the percent variance explained as a function of the number of clusters (**Fig 2E**, see methods). Unexpectedly, the committee converged on a *k* of four classes for each classification scheme instead of the two, as predicted by the literature, with 8 out of 20 indices converging four classes with the next highest k predictions only receiving 3 or less votes. (**Fig 2F**). Supporting this finding, all four classification methods (Feature Selection, DTW, agglomerative and divisive hierarchical clustering) classified 96.3% of n = 733 exocytic events exocytic events unanimously. Therefore the differences between events and between clusters

were sufficiently robust to be discerned via multiple methods **(Fig 2G).** Inspection of events with conflicting classification revealed edge cases, with either low signal-to-noise or occurrence close to or on the cell periphery **(Fig 2G, inset).** All four classes were sensitive to tetanus neurotoxin (TeNT, **Fig 2H**), which cleaves VAMP2 and blocks VAMP2-mediated SNARE complex formation and fusion (Link et al., 1992). This indicates that all four classes contain bona fide exocytic events.

Distinguishing features of four modes of exocytosis

We next sought to characterize the four classes of exocytosis (**Fig 3**). Class averages and representative image sequences revealed distinct fluorescence profiles (**Fig 3A**). Class 1 and 2 exhibited an instantaneous fluorescence decay after peak ΔF/F (fusion pore opening). In contrast, class 3 and 4 exhibited a delay between peak ΔF/F and the onset of fluorescent decay, observed as a plateau in ΔF/F prior to fluorescence decay (**Fig 3A**).

A single exponential decay fit well to the fluorescence decay in classes 1 and class 2 events (**Fig 3B**), but was a poor fit for classes 3 and 4 (**Fig 3C**). The "delay" between peak ΔF/F and onset of decay in class 3 and 4 events accounted for the poor fit, and fitting sequential exponentials resulted in a higher R^2 (**Fig 3D**). All half-life estimations for class 3 and 4 were thus made after fitting sequential exponentials to events with a delay and measuring the second exponential. After decay onset, there were no differences in half-life between class 1 and 3 or class 2 and 4 (**Fig 3E**), suggesting the mechanism of fluorescence decay is the same for classes 1 and 3 and for classes 2 and 4.

Loss of fluorescence following KNR presumably is due to vesicle-reacidification, whereas loss of fluorescence following FVF is due to VAMP2-pHluorin diffusion. Therefore, increasing buffering capacity of the vesicle lumen is predicted to slow fluorescence decay rate in KNR but not FVF. Only the half-life of classes 2 and 4 exhibited a HEPES-sensitive increase in $t_{1/2}$ (**Fig 3E**), suggesting they represent KNR-like classes. We next measured the VAMP2-pHluorin fluorescence in pixels surrounding each exocytic event ROI (**Fig 3F**). Fluorescence was not detected at the border of HEPES sensitive events (class 2 and 4, **Fig 3F,G**). The pixels surrounding class 1 and 3 events exhibited a fluorescent peak followed by an exponential decay with the same $t_{1/2}$ as the center pixels of the events **(Fig 3H)**, consistent with fluorescence decay caused by diffusion**.** Since classes 1 and 3 were not HEPES sensitive, yet exhibited diffusion of VAMP2-pHluorin fluorescence into surrounding pixels (**Fig 3F-H**), these classes are consistent with FVF-like exocytic events. Based on these observations and either the instantaneous (i) or delayed (d) onset of fluorescence decay after peak ΔF/F, we named the classes FVFi, (class 1), KNRi (class 2), FVFd (class 3), and KNRd (class 4).

Expression of a truncated VAMP2 alters exocytic mode

To investigate whether our classifier was potentially distinguishing exocytic classes based on fusion pore behavior, we turned to expression of a tagRFP-VAMP2 construct lacking the transmembrane domain ($VAMP2^{1-96}$, **Fig 4A**) along with VAMP2-pHluorin. Capacitance measurements demonstrated that expression of $VAMP2^{1-96}$ stabilizes fusion pores with a narrow diameter that do not transit to full fusion (Guček et al., 2016). We found that $VAMP2^{1-96}$ expression reduced the frequency of exocytic events in both soma and neurites (**Fig 4B**). Intriguingly, $VAMP2^{1-96}$ specifically reduced the frequency of FVFi and FVFd events, without affecting the frequency of KNRi and KNRd (**Fig 4C**). This shifted the distribution of exocytic

events toward KNRd and KNRi (**Fig 4D**), aligning with capacitance measurements (Guček et al., 2016). Even though the diffraction limited resolution of our microscope obfuscates visualization of the fusion pore properties other than opening, alignment with capacitance measures supports the hypothesis that the visualized delay in fluorescence decay is either a delay in fusion pore dilation (FVFd) or delay in fusion pore closure (KNRd). That VAMP2$^{1-96}$ specifically decreases the frequency of FVFi and FVFd and not KNRi and KNRd, suggests that the FVF-like classes may be mechanistically distinct from KNR.

TRIM67 biases exocytic mode towards full-vesicle fusion

Although our experiments with TeNT (**Fig 2H**), HEPES (**Fig 3E**), VAMP2-tagRFP (**Fig 1F**), and VAMP2$^{1-96}$ (**Fig 4**) support the conclusion that each exocytic class harbors bona fide and distinct exocytic events, the biological relevance of individual modes and molecular mechanisms influencing exocytic modes are unclear. Our previous work identified the E3 ubiquitin ligase TRIM9 as a novel regulator of neuronal exocytosis (Urbina et al., 2018; Winkle et al., 2014). We found that TRIM9 reduced SNARE complex formation, thus reducing the frequency of vesicle fusion. Although deletion of *Trim9* elevated the frequency of exocytosis (Urbina et al., 2018; Winkle et al., 2014), using the classifiers we found that deletion of *Trim9* did not change the ratio of exocytic classes **(Fig 5A)**. Thus TRIM9 specifically regulates the frequency and not the mode of fusion. TRIM67 is a TRIM9 paralog also enriched in developing neurons (Boyer et al., 2018); we tested its potential role in regulating exocytosis. Unlike *Trim9*, deletion of *Trim67* did not alter the frequency of exocytosis (**Fig 5B**). However, it did alter the mode of exocytosis; KNRi and KNRd increased two-fold, whereas FVFi and FVFd decreased (**Fig 5A**). This supports the hypothesis that exocytic mode and frequency can be distinctly regulated. We compared the distributions of exocytic classes within soma or neurites; the distribution in the soma was not distinct from the whole neuron, however FVFd events were enriched in neurites. This was not altered by deletion of *Trim67* (**Fig 5C**).

During neuronal morphogenesis neuronal surface area increases (**Fig 5D**). Our previous experimental and modeling work demonstrated that VAMP2-mediated exocytosis provided excess material for plasma membrane expansion in developing neurons, which was partially balanced by clathrin-mediated endocytosis (Urbina et al., 2018) (**Fig 5E**). To build this model, empirically measured sizes of non-coated and clathrin-coated vesicles were combined with measured frequencies of exocytosis and endocytosis. A caveat of these calculations was the assumption that all VAMP2-mediated exocytic events supplied plasma membrane material. Upon considering that KNRi and KNRd comprise ~22% of events (**Fig 5A**), we sought to update our model with the distribution of exocytic modes (**Fig 5F**). Basal surface areas of neurons expressing GFP-CAAX were measured at 24 and 48 h *in vitro* via TIRF microscopy, and were used to estimate neuronal surface area (**Fig 5D**, see methods) as a ground truth baseline. Based on these data, we simulated the surface areas of a population of 1000 neurons at 24 h (SA_{24} (x)). We then modeled net membrane addition to this simulated population, accounting for vesicle sizes, exocytic frequency and mode, and endocytic frequency (**Fig 5F,G**). At the end of the 24 h period, a population of neurons that had increased in surface area was compared to empirical measurements of neuron surface area at 48 h *in vitro* (**Fig 5H**). This demonstrated that accounting for KNRi and KNRd in surface area expansion improved the similarity of predictions to true measured values of surface area (**Fig 5H vs 5E**), suggesting an appropriate model for predicting neuronal growth. We expanded our simulation to 72 h (**Fig 5I**). The modeled neurons

matched the measured surface area well, however a population of neurons with larger surface areas arose at 72 h *in vitro* that were not reflected in the simulated data.

Since deletion of *Trim67* decreased FVFi and FVFd and increased KNRi and KNRd, we simulated growth of *Trim67*$^{-/-}$ neurons using this ratio of modes and estimated surface areas at 24 h (**Fig 5J**). This predicted surface area expansion to decrease from ~868 μm^2 to 540 μm^2. The measured basal surface area of *Trim67*$^{-/-}$ neurons was reduced, agreeing with the prediction. This suggests that a bias in mode of exocytosis is sufficient to decrease surface area. When extended to 72 h, the reduction in surface area of *Trim67*$^{-/-}$ neurons compared to *Trim67*$^{+/+}$ neurons was greater (both simulated and measured, **Fig 5K**). This would predict that *Trim67*$^{-/-}$ neurons have a decelerated morphogenesis. Indeed at five days in vitro, *Trim67*$^{-/-}$ neurons had decreased axon length (**Fig 5L**). Simulations of a population of *Trim9*$^{-/-}$ neurons based on empirical basal surface area measurements with the increased exocytic frequency of *Trim9*$^{-/-}$ neurons predicted increased neuronal surfaces areas, which was confirmed by measured surface areas at 48 and 72 h (**Fig 5M**). Intriguingly, our *Trim9*$^{-/-}$ simulations were a poorer fit to empirically measured neuronal surface area, overestimating the increase in neuron size. This suggests that compensatory mechanisms may temper net membrane addition. While this model makes a number of assumptions, including that vesicles fusing via different modes are the same size and that vesicles sizes and rates of endocytosis are not altered by deletion of *Trim9* or *Trim67,* the remarkable fit between simulated and empirically measured data suggests that we have captured the most relevant factors responsible for developmental neuronal growth.

The t-SNARE SNAP47 interacts with TRIM67 and localizes to VAMP2-mediated exocytic events

We next sought to determine how TRIM67 altered exocytic mode. Time-lapse TIRF microscopy revealed that TRIM67 did not localize to VAMP2-mediated exocytic events (**Fig 6A**). To confirm that changes in exocytic modes were due to loss of TRIM67, we introduced full length, RFP-tagged TRIM67 into *Trim67*$^{-/-}$ neurons **(Fig S1A)**. This rescued the ratio of exocytic modes (**Fig S1B**) without changing the frequency of exocytosis (**Fig S1C**). These data indicate TRIM67 biases the mode of exocytosis toward FVFi and FVFd and away from KNRi and KNRd, but likely does so remotely, via an intermediary. TRIM67 is a TRIpartite Motif (TRIM) E3 ubiquitin ligase, characterized by a ubiquitin ligase RING domain, two BBox domains, a coiled-coil motif (CC) that mediates multimerization, a COS domain, FN3 domain, and SPRY domain (**Fig S1A**). As TRIM67 is a relatively unexplored protein, few binding partners have been identified. Further complicating this, E3 ligases typically exhibit transient interactions with binding partners.

To identify potential interacting partners for TRIM67 in neurons that may regulate exocytosis, we transduced cortical neurons with a herpes virus carrying Myc-BirA*TRIM67ΔRING to perform proximity biotinylation followed by mass spectrometry of biotinylated proteins (See Methods)(Roux et al., 2012). This approach is ideal as it allows identification of transient interactions. Although the full catalog of hits from this proteomic approach will be reported elsewhere (Menon et al., in preparation), one interesting candidate significantly enriched (~4 fold) over the negative control (Myc-BirA*, Supplementary Table 1) was SNAP47, a t-SNARE homologous to SNAP25. SNAP47 forms thermally stable SNARE complexes and competes with SNAP25 at equimolar amounts in vitro for formation of SNARE complex (Holt et al., 2006). Although SNAP47-containing SNARE complexes are capable of fusion, they are significantly less efficient in liposomal fusion assays (Holt et al., 2006).

To validate an interaction between TRIM67 and SNAP47, we performed co-immunoprecipitation assays using epitope tagged proteins expressed in HEK293 cells (**Fig 6B**). Myc-SNAP47 co-precipitated GFP-TRIM67, but not GFP-TRIM9, confirming that TRIM67 and SNAP47 interact. Consistent with an interaction in neurons, live TIRF microscopy revealed that TRIM67-GFP puncta colocalize with SNAP47-tagRFP, particularly at the periphery of neurons (**Fig 6C, arrows**). Unlike TRIM67 however, time-lapse TIRF microscopy revealed that SNAP47 co-localized with a subset (28%) of VAMP2-pHluorin exocytic events (**Fig 6D**). Considering exocytic events are distributed throughout the basal surface of the neuron, this suggests that SNAP47 and TRIM67 potentially interact at sites distal from exocytic events.

Multiple domains and ligase activity of TRIM67 modulate the interaction with SNAP47 and exocytic mode

These data suggested that SNAP47 is poised to be the intermediary regulating exocytic mode. To determine domains of TRIM67 important for interacting with SNAP47, we performed co-immunoprecipitation assays using TRIM67 domain mutants expressed in *TRIM67*$^{-/-}$ HEK293 cells (Boyer et al., 2018)(**Fig 6E**). Similar structure:function experiments were performed in *Trim67*$^{-/-}$ neurons to examine exocytic mode using RFP-TRIM67 domain mutants (**Fig S1B,C**). MycTRIM67ΔFN3 failed to precipitate detectable levels of GFP-SNAP47 (**Fig 6E**), and failed to rescue the ratio of exocytic modes (**Fig S1B**). MycTRIM67ΔSPRY precipitated similar amounts of GFP-SNAP47 compared to TRIM67 and similarly rescued exocytic mode (**Fig 6E, S1B**), indicating the SPRY domain is dispensable for both SNAP47 interaction and exocytic mode. In contrast, more SNAP47 was detected in MycTRIM67ΔRING and MycTRIM67ΔCC, yet these mutants failed to rescue the ratio of exocytic modes. Similarly mutation of conserved Zn-coordinating cysteines in the ligase domain required for ligase activity (TRIM67LD,(Boyer et al., 2020) failed to rescue exocytic mode (**Fig S1B**). None of these mutants altered the overall frequency of exocytosis (**Fig S1C**). Deletion of the COS domain (TRIM67ΔCOS) however exhibited a unique phenotype; it decreased the frequency of exocytosis, but did not rescue the ratio of exocytic modes (**S1B,C**). Interestingly, MycTRIM67ΔCOS precipitated much more GFP-SNAP47 (**Fig 6E**). Together these structure:function experiments are consistent with the hypothesis that a transient interaction between TRIM67 and SNAP47 may regulate exocytic mode.

TRIM67 alters exocytosis via modulated SNAP47 protein levels

We next examined SNAP47 protein levels in *Trim67*$^{+/+}$ and *Trim67*$^{-/-}$ neurons (**Fig 7A**). This revealed a 1.5x fold increase in SNAP47 protein in *Trim67*$^{-/-}$ neurons, suggesting TRIM67 regulates SNAP47 expression or stability. A cyclohexamide chase in *Trim67*$^{+/+}$ and *Trim67*$^{-/-}$ cortical neurons revealed that SNAP47 was degraded at the same rate (**Fig S2A**). Bortezamide or chloroquine treatments indicated SNAP47 degradation in both genotypes was proteasome-dependent and lysosome independent (**Fig S2A**). To determine if TRIM67 regulated SNAP47 via ubiquitination, we performed denaturing immunoprecipitation of GFP-SNAP47 in *TRIM67*$^{-/-}$ HEK293 cells co-expressing HA-ubiquitin and either Myc or Myc-TRIM67 **(Fig S2B)**. HA-ubiquitin that co-immunoprecipitated with GFP-SNAP47 and migrated at a higher apparent molecular weight was interpreted as ubiquitinated SNAP47 (SNAP47-Ub). However we did not detect changes in the ratio of SNAP47-Ub:SNAP47, suggesting that TRIM67 is not required for SNAP47 ubiquitination. Altogether, these results suggest that TRIM67 does not alter the

proteasomal-dependent degradation of SNAP47, suggesting a more complex regulation SNAP47 by TRIM67.

Although the mechanism elevating SNAP47 protein is unknown, we hypothesized that the elevated SNAP47 in *Trim67*$^{-/-}$ neurons may alter the ratio of exocytic modes. Like deletion of *Trim67* (**Fig 5B**), overexpression of SNAP47 in *Trim67*$^{+/+}$ neurons did not alter the frequency of exocytosis (**Fig 7B**). However, overexpression of SNAP47 did increase KNRd and KNRi events (**Fig 7C**). Strikingly, it also increased the delay time before onset of fluorescent decay in both KNRd and FVFd (**Fig 7D**), which was specifically pronounced when SNAP47-tagRFP was detectable at the fusion site (red data points). Once fluorescence decay initiated, overexpression of SNAP47 did not affect the half-life (**Fig. 7E**). These findings indicated increased SNAP47 promotes KNRd, and is thus sufficient to shift exocytic mode.

To determine if increased SNAP47 levels were required to shift exocytic mode in *Trim67*$^{-/-}$ neurons, we reduced SNAP47 protein levels using siRNA (**Fig 7F, F'**). Knockdown of SNAP47did not alter the frequency of exocytosis (**Fig7G**), but decreased KNRd and KNRi and increased FVFi and FVFd (**Fig 7H**). This suggests that increased SNAP47 shifts the mode of exocytosis in *Trim67*$^{-/-}$ neurons.

SNAP47 forms more SNARE complexes in *Trim67*$^{-/-}$ neurons

The increase in SNAP47 protein in *Trim67*$^{-/-}$ neurons and the exocytic phenotypes associated with SNAP47 overexpression and knockdown suggested that in *Trim67*$^{-/-}$ neurons, SNAP47 may alter exocytosis by forming more SNARE complexes with VAMP2. To test this, we compared SDS-resistant, thermally-stably SNARE complexes in *Trim67*$^{+/+}$ and *Trim67*$^{-/-}$ neurons, which run at higher molecular weights than their monomeric constituents. To enhance SNARE complex detection, neurons were treated with NEM to reduce disassembly or treated with NEM and DTT, which would not impair SNARE disassembly. VAMP2, SNAP25, and syntaxin-1 exhibited similar proportions of high molecular weight species:monomer between genotypes. In contrast, *Trim67*$^{-/-}$ neurons exhibited increased amounts of higher molecular weight SNAP47 relative to monomer (**Fig 8A,B**), suggesting increased SNAP47-containing SNARE complexes were present in *Trim67*$^{-/-}$ neurons. This suggests that TRIM67 inhibits the incorporation of SNAP47 into SNARE complexes and thus, SNAP47-mediated fusion events. Endogenous immunoprecipitation of SNAP47 from membrane fractions of *Trim67*$^{+/+}$ and *Trim67*$^{-/-}$ neurons showed that SNAP47 interacted with both syntaxin-1 and VAMP2 (**Fig 8C**), consistent with SNARE complex formation. VAMP2 co-precipitated with SNAP47 ~1.5-2x more in *Trim67*$^{-/-}$ neurons, further supporting the hypothesis that deletion of *Trim67* increases SNAP47 incorporation into exocytic SNARE complexes with VAMP2. **(Fig 8C**).

Discussion

Here we developed a novel, unbiased, and unsupervised set of classifiers to identify four distinct classes of TeNT-sensitive, *bona fide* exocytic events in developing cortical neurons. Distinct mechanisms of VAMP2-pHluorin fluorescence decay that were either HEPES sensitive or diffusion-dependent suggested that two classes were KNR-like and two classes were FVF-like. The delayed or instantaneous onset of fluorescence decay after fusion pore opening (peak $\Delta F/F$) further distinguished exocytic classes into KNRd, KNRi, FVFd, and FVFi. We found that the E3 ubiquitin

ligase TRIM67 regulated the mode of exocytosis; genetic deletion of *Trim67* increased KNRi and KNRd and decreased FVFi and FVFd. Our data support the hypothesis that TRIM67 alters exocytic mode in part by regulating SNAP47 protein level and consequently incorporation into SNARE complexes. In the absence of TRIM67, SNAP47 protein levels and SNAP47 incorporation into SNARE complexes increased. Finally our data suggest that SNAP47 may temporarily arrest the fusion pore in an open state.

Distinguishing exocytic modes with novel classifiers and protein perturbation

Distinguishing modes of exocytosis is not a simple task, as exocytosis is temporally fast and spatially small, the average fusion pore size being roughly 1-5 nm (Albillos et al., 1997; Bao et al., 2018). Although semi-automated classification algorithms of vesicle fusion events exist, they are supervised classification schemes, requiring input to determine ground truth classes (Diaz et al., 2010; Yuan et al., 2015). In contrast, our classifier requires no *a priori* information. Instead automated exocytic detection coupled with feature extraction with PCA, hierarchical clustering, and dynamic time warping, in conjunction with a clustering indices delivered the surprising finding that four classes of exocytic events exist in developing cortical neurons: FVFi, FVFd, KNRi, and KNRd. These four classes are biologically relevant, as their relative proportions are regulated by TRIM67 and SNAP47. Of note, altering the half-life of these events with HEPES did not alter the classification of events or frequency of different exocytic modes. This exemplifies the robustness of the classification system and the benefits of classifying exocytic events using multiple features.

Defining KNR as a distinct mode from FVF at the synapse remains controversial, relying on indirect evidence to suggest the vesicle does not collapse into the plasma membrane (He and Wu, 2007; Alabi and Tsien, 2013; Karatekin, 2018). Using developing neurons and their unique spatial distribution and temporal frequency of exocytosis, we resolved individual events, allowing identification of not two, but four discrete classes. Some classes are characterized by a delay after fusion, in which fluorescence does not decay instantaneously. This delay may represent the fusion pore stabilized in an open state, which may facilitate the release of larger cargo. This is supported by the expression of a VAMP2 peptide which is known to stabilize the fusion pore (Guček et al., 2016). Alternatively, the delay may represent a decision point for the fusion state, prior to the vesicle undergoing FVF or KNR. Finally the delay could represent an inefficiency in fusion, as the opening and dilation of the fusion pore is an energy barrier that must be overcome by SNARE machinery (Chernomordik and Kozlov, 2008).

Exocytic mode and morphogenesis

Distinct modes of exocytosis potentially suggest roles for exocytosis in developing neurons beyond neurotransmitter release. Pre-synaptogenesis, exocytosis takes on cell-building roles, providing membrane materials to the expanding plasma membrane (Pfenninger, 2009). A developing neuron, therefore, may maximize FVF and membrane addition via exocytosis. In contrast in a mature neuron that is not expanding the plasma membrane secretion via KNR may be more relevant. Using our powerful classification tool, we found that FVFi events comprised most exocytic events in developing neurons, indicating that the majority of exocytic events in developing neurons were membrane adding. This suggests that membrane addition is favored during early neuron development, and is supported by the finding that decreasing the amount of FVF relative to KNR associated with deletion of *Trim67* in developing neurons resulted in a significantly reduced surface area. This link between exocytic mode and morphogenesis suggests that tight spatial and temporal control of exocytosis is

needed for proper neuron development. Interestingly, TRIM67 protein levels drop in the mature cortex once morphogenesis is complete, potentially supporting the hypothesis that KNR-like modes of exocytosis increase at later developmental stages (Boyer et al., 2018).

Simulations of neuronal growth, considering the frequency and mode exocytosis, the frequency of endocytosis, and the size of respective vesicles, remarkably recapitulated the developmental increase in neuronal surface area at 48 h *in vitro*, fitting better than simulations assuming all fusion events were FVF. Altering exocytic mode or frequency in model simulations to mimic *Trim67*$^{-/-}$ or *Trim9*$^{-/-}$ neurons predicted altered membrane addition and surface areas, which were supported by empirical measurements. This agreement suggests that although our model is simple, it captures relevant parameters and accurately predicts changes in surface area. We conclude that VAMP2-mediated fusion is the primary source of surface area expansion in developing neurons, and that manipulating exocytic frequency or mode alters neuronal growth. Interestingly, the surface area of neurons at 72 h was multi-modal; information not captured in our model. This potentially suggests in a subset of neurons, additional parameters are involved in plasma membrane expansion, such as membrane added via ER-plasma membrane contact sites or exocytosis mediated by other SNARE proteins such as VAMP7 (Fuschini et al., 2018; Galli et al., 1998) that may improve our prediction accuracy. Alternatively, these other modes in surface area may represent distinct neuronal sub-populations, such as pyramidal or inhibitory neurons, that increase their surface area at different rates (Fuschini et al., 2018).

Two TRIM proteins regulate exocytic membrane addition via distinct mechanisms

Phylogenetic analysis of class I TRIM proteins revealed that *Trim67*, a closely related paralog of *Trim9*, is the closest vertebrate TRIM similar to the single invertebrate class 1 TRIM9/67 in *Drosophila* and *C. elegans* (Boyer et al., 2018). Both TRIM67 and TRIM9 share identical domain organization and 63.3% sequence identity (Short and Cox, 2006). However, they exhibit contrasting expression patterns during murine cortex development, with TRIM67 expression peaking late embryonically and early perinatally, whereas TRIM9 expression peaks in the adult (Boyer et al., 2018). TRIM67 and TRIM9 both interact with the netrin-1 receptor DCC, and they heterodimerize, suggesting they may regulate similar neuronal pathways (Boyer et al., 2018).

In developing neurons, TRIM9 interacts with t-SNARE SNAP25 and reduces the frequency of exocytosis (Urbina et al., 2018; Winkle et al., 2014). Interestingly, TRIM67 interacts with a homologous t-SNARE SNAP47 and alters the mode of exocytosis. Our previous work suggested TRIM9 reduced exocytic frequency via constraining formation of SNAP25 containing SNARE complexes, which did not involve TRIM9-dependent ubiquitination of SNAP25 (Urbina et al., 2018; Winkle et al., 2014). Analogously, TRIM67 regulates exocytic mode by limiting SNAP47 incorporation into SNARE complexes, and this also appears to be independent of SNAP47 ubiquitination. Although changes in SNARE ubiquitination were not observed in either case, ligase activity of both TRIM9 and TRIM67 were required for their exocytic regulation. Genetic deletion of *Trim9* removed constraint on SNAP25 incorporation into SNARE complexes, which lead to an increased frequency of exocytosis (Winkle et al., 2014), whereas genetic deletion of *Trim67* increased incorporation of SNAP47 into SNARE complexes, changing the mode or exocytosis. The increased exocytic frequency that occurs with deletion of *Trim9* leads to aberrant axonal branching during development (Winkle et al., 2014), presumably at least partially due to increased membrane

addition. Deletion of *Trim67*, in contrast, leads to reduced axon length, presumably due to reduced membrane addition caused by decreased FVF. Therefore, TRIM9 attenuates membrane addition through regulating the constitutive rate of exocytosis, whereas TRIM67 promotes FVFi and FVFd at the expense of KNRi and KNRd. Interestingly, the TRIM9-SNAP25 interaction and constraint on exocytic frequency was reversed by the axon guidance cue netrin (Winkle et al., 2014). As TRIM67 also interacts with the netrin receptor DCC (Boyer et al., 2018), this suggests that netrin may affect exocytic mode. The opposing functions and expression patterns of TRIM67 and TRIM9 may help orchestrate the complex development of a neuron: during early neuronal development, high levels of TRIM67 maximize modes of exocytosis that increase membrane expansion. In a mature neuron, however, high TRIM9 levels may suppress constitutive exocytosis, and lower TRIM67 levels may promote KNRi and KNRd, potentially at the synapse.

TRIM67 regulates exocytic mode via SNAP47

Our observations that TRIM67 did not colocalize with VAMP2-mediated events yet deletion of *Trim67* altered the mode of VAMP2-mediated exocytosis, suggests TRIM67 regulates exocytic mode distal to fusion sites. Observations that TRIM67 interacted with and colocalized with SNAP47 distal to exocytic sites, and that SNAP47 co-localized with a subset of VAMP2 pHluorin events with distinct fusion parameters fit with a hypothesis that TRIM67 regulated exocytic mode via SNAP47. Structure function assays suggests this interaction likely must be transient to appropriately regulate fusion mode. Although we do not yet understand how TRIM67 regulates SNAP47 protein, our data suggest that altered SNAP47 protein levels and altered incorporation into exocytic SNARE complexes was necessary and sufficient to alter fusion pore kinetics and exocytic mode. Given that manipulation of SNAP47 levels altered the amount of KNRd, we hypothesize that the SNAP47-containing SNARE complexes may be the primary SNARE complex involved in KNRd.

Regulation of fusion pore kinetics and mode of exocytosis by regulatory proteins and number of SNAREs are well-documented (Bao et al., 2018; Bretou et al., 2014; Gauthier et al., 2011; Wen et al., 2016; Logan et al., 2017; Segovia et al., 2010; Archer et al., 2002) but SNARE complex composition adds another layer of regulation. Our findings suggest that regulation of modes of exocytosis in developing neurons is facilitated by incorporation of SNAP47, a member of the SNAP25 family of Qb/Qc t-SNAREs, into SNARE complexes. SNAP47 is capable of substituting for SNAP25 to form stable SNARE complexes with VAMP2 and syntaxin-1 using purified recombinant proteins. These complexes however, are inefficient in liposomal fusion assays, suggesting that fusion is slow to proceed in comparison to SNAP25 containing SNARE complexes (Holt et al., 2006). Interestingly SNAP47 has many unique features that may be responsible for altered fusion kinetics: it lacks cysteine palmitoylation-mediated membrane targeting, has a long N-terminal extension, and a linker region between the Qb and Qc SNARE domains (Holt et al., 2006). Even without palmitoylation sites, SNAP47 associates with the membrane, and co-fractionates with synaptic vesicles (Holt el al., 2006).

Other mechanisms that may alter exocytic mode

As overexpression or knockdown of SNAP47 does not fully recapitulate the exocytic phenotype of *Trim67*$^{-/-}$ neurons, TRIM67 may orchestrate regulation of exocytosis via multiple mechanisms. Myosin II, actin remodeling at the plasma membrane, and membrane tension are all suggested to alter exocytosis (Aoki et al., 2010; Wen et al., 2016). TRIM67 interacts with the actin-

polymerase VASP at the growing tips of filopodia in the growth cone, a highly dynamic region with local changes in membrane tension and actin remodeling (Boyer et al., 2020; Staykova et al., 2011; Wen et al., 2016), but whether VASP alters exocytosis is not known. There are a host of proteins that may regulate exocytic mode, such as Cdc42 , a-synuclein, synaptotagmins (Bretou et al., 2014; Gauthier et al., 2011; Wen et al., 2016; Logan et al., 2017; Segovia et al., 2010). Separate pools of vesicles have been distinguished based on their fusion characteristics and cargo, and different vesicle populations may fuse with different modes of fusion (Hua et al., 2011; Rizzoli and Jahn, 2007). Future work must define how TRIM67 interfaces with these vesicle populations and distinct mechanisms regulating fusion, and whether this unique regulation occurs at the synapse or is specific to earlier developmental time points.

Figure 1

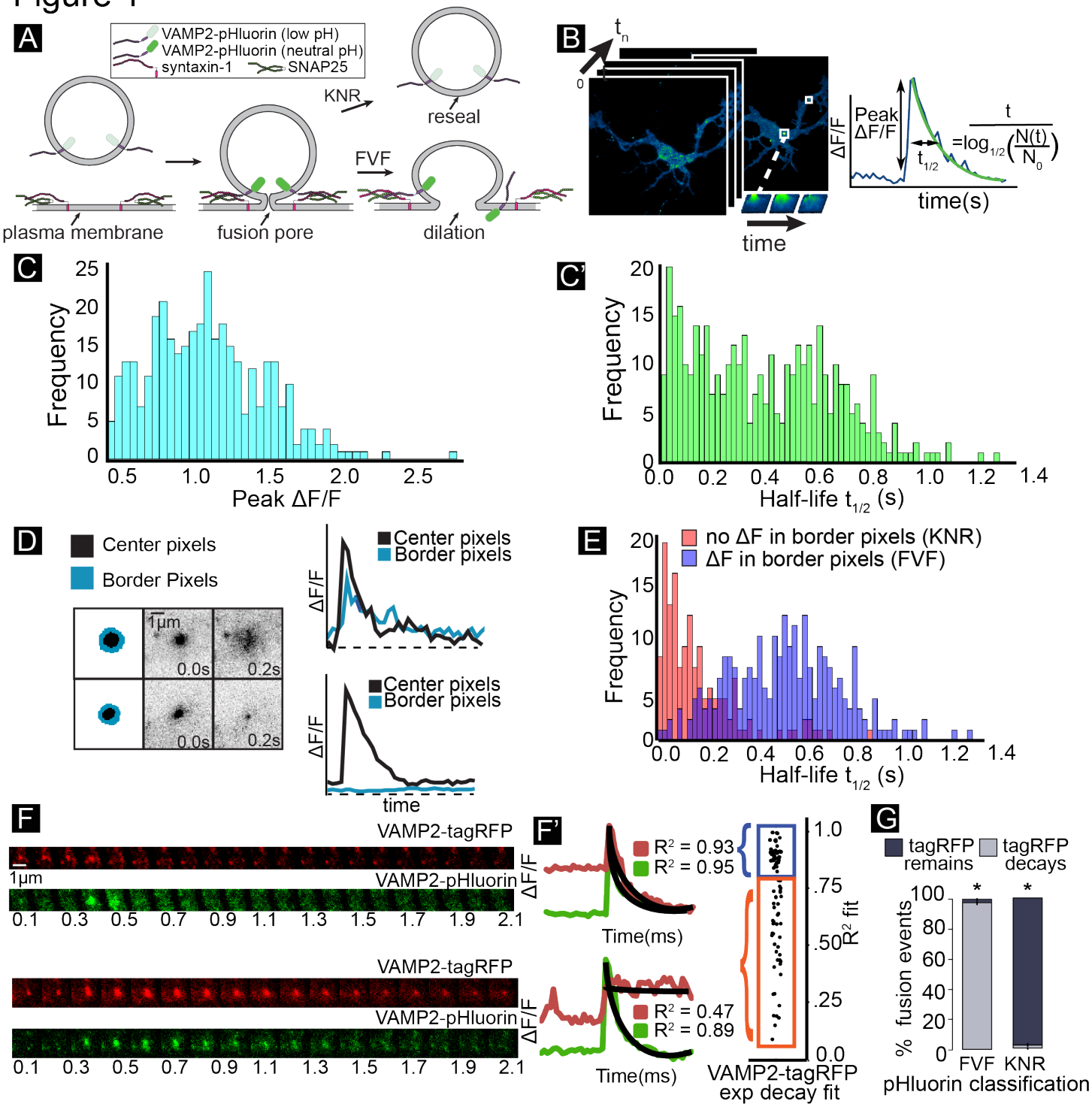

Figure 1. Heterogeneity in single vesicle exocytic fusion events. A) Schematic of exocytic fusion depicts quenching and fluorescence of VAMP2-pHluorin. pHluorin is quenched in the vesicle lumen and fluoresces upon fusion pore opening. Subsequently the fusion pore either dilates during full vesicle fusion (FVF) and fluorescent VAMP2-pHluorin diffuses within the plasma membrane, or the pore reseals during Kiss-and-run fusion (KNR) and VAMP2-pHluorin is quenched by vesicle reacidification. **B)** Diagram of automated detection of exocytosis. Exocytic events (green) are detected over time. Features are extracted from events, including the peak ΔF/F and half-life of fluorescence. Frequency of **C)** peak ΔF/F and **C')** fluorescence half-life of individual events. **D)** Schematic of region

of exocytic event (black) and surrounding border pixels (blue). Plots of ΔF/F over time demonstrate an event with subsequent spreading of fluorescence into border pixels (top, FVF), and an event that without spreading of fluorescence (bottom). **E)** Frequency of half-life categorized by ΔF in border pixels. Spreading fluorescence events (ΔF, presumbably FVF) have a slower fluorescence decay than those without (no ΔF, presumably KNR). **F)** Dual-color time lapse imaging of VAMP2-pHluorin and VAMP2-tagRFP reveals vesicle fusion events and vesicle fate, respectively. Example images and ΔF/F curves shows that VAMP2-tagRFP either exponentially decays after ΔF/F (top, FVF) or remains in retained vesicle (bottom, KNR). **G)** Classification of fusion events based on VAMP2-pHluorin behavior or VAMP2-tagRFP behavior agree. * represents P-value < 0.05 based on a chi-squared analysis of expected ratios if the classes were assigned randomly.

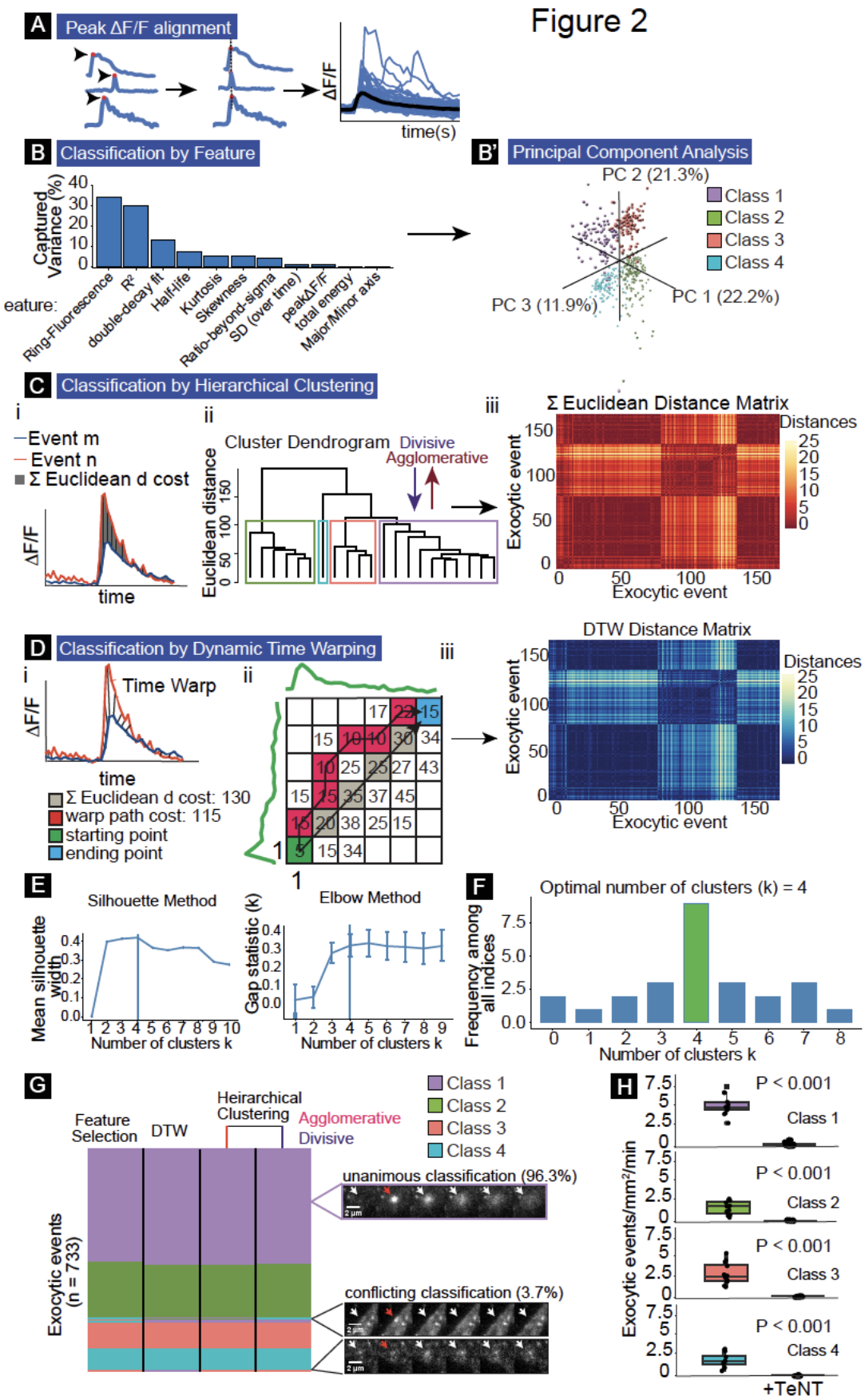

Figure 2: Multiple unbiased classifiers converge on four exocytic modes. A) After automated detection, ΔF/F curves are temporally registered to peak ΔF/F (red dot). ΔF/F plotted over time showing time registered average

(black) and individual events (blue). **B)** Features that represent 85% of captured variance from PCA. **B')** Three principal components plotted revealing four exocytic classes. **C)** Event classification by hierarchical clustering. i) ∆F/F plotted over time depicting the summed (∑) Euclidean distance between two exocytic events, m and n. ii) Dendrogram of ∑ Euclidean distances between multiple events, linked by agglomerative or divisive hierarchical clustering revealing four exocytic classes. iii) Each pixel in distance matrix is the ∑ Euclidean distance between two ∆F/F curves (n=733). **D)** Event classification by Dynamic Time Warping (DTW). i) ∆F/F plotted over time depicting time warped distance between two exocytic events, m and n. ii) A matrix of Euclidean distances measured at all time point comparisons of a pair of exocytic events, starting at peak ∆F/F (green square, co-ordinates 1,1). Unlike the ∑ Euclidean distance (gray), DTW uses the warp path with the lowest cost (red squares) is found through the matrix to reach the ending point (blue square). The sum of the total warp path is the DTW distance per pair of exocytic events. iii) Each pixel in distance matrix is the total DTW cost between two ∆F/F curves (n = 733). **E)** Two example indices used in the plurality rules committee. Both the silhouette and elbow method suggest four exocytic classes. **F)** Decision histogram of the committee of indices, with the plurality of indices choosing four exocytic classes (8/20). **G)** Classification comparison of each of the methods of clustering. 96.3% of 733 events were classified unanimously. Purple inset: representative unanimously classified exocytic event. Black inset: representative exocytic events with conflicting classification. Cell edge effects (top black inset) or low signal-to-noise ratio (bottom black inset) account for the majority of conflict. White arrows denote exocytic events. Red arrow denote peak ∆F/F. **H)** Frequency of all event classes drops to near zero with tetanus toxin (TeNT) treatment (t-test, n = 12 cells per experiment).

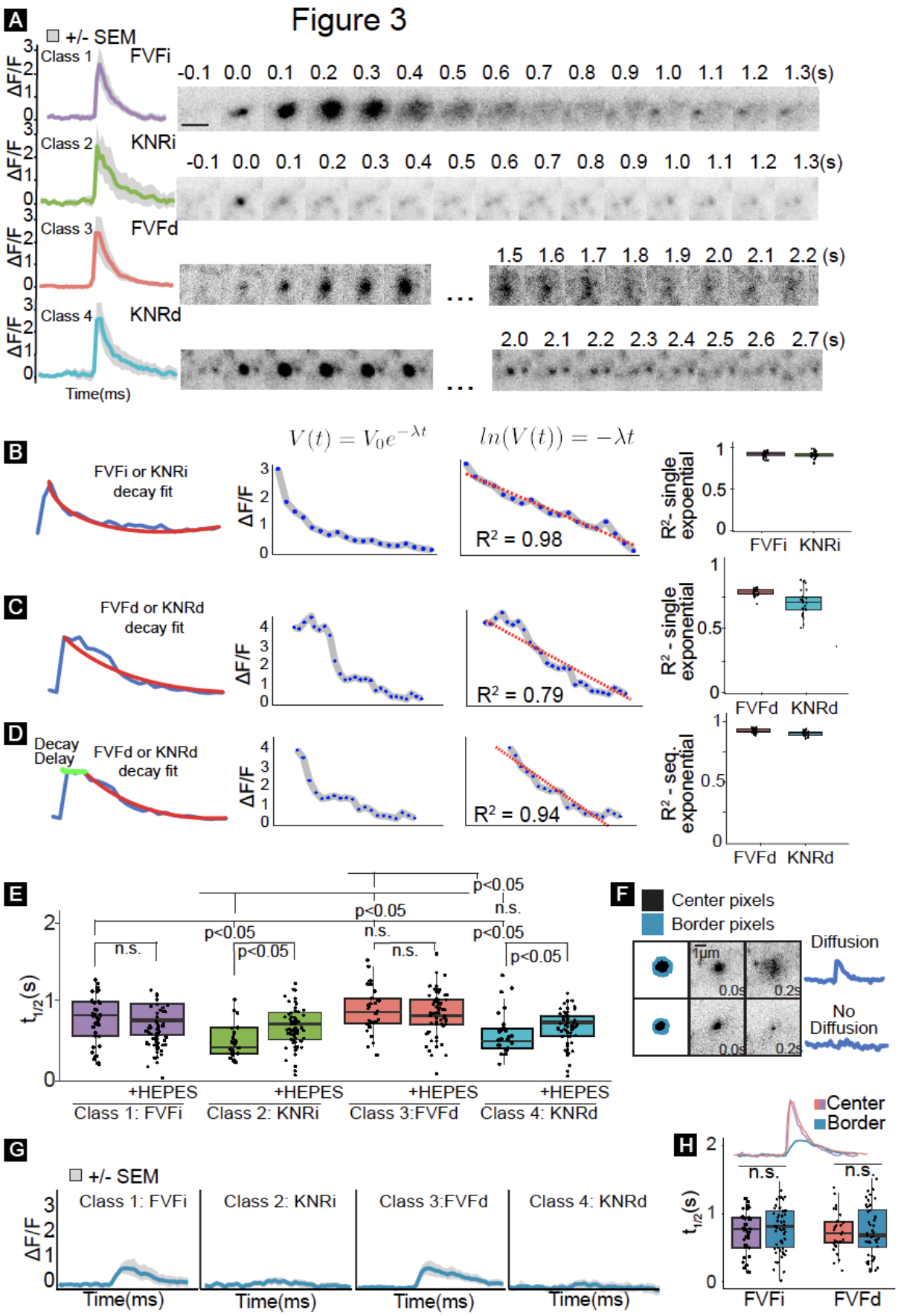

Figure 3: Distinguishing features of four modes of exocytosis. A) Mean fluorescent curves +/- SEM (grey) and

representative images from each class (right). **B-C)** Example single exponential decay fit ($V(t) = V_0e^{-\lambda t}$) to a class 1 or 2 instantaneous (i) events (B) or to class 3 or 4 delay (d) events (C). The log of an exponential decay curve ($\ln(V(t))=-\lambda t$) is linear, and the linear regression fit (R^2) is an indicator of how good of a fit the exponential decay curve is (center graph). Box plots (right) of R^2 of class 1 (FVFi) and class 2 (KNRi) events show a good fit (B) whereas fit to class 3 (FVFd) and class 4 (KNRd) are poor. **D)** Fitting sequential exponential decay curves provides a better fit to FVFd and KNRd. **E)** Half-life of fluorescence decay ($t_{1/2}$) of each class untreated or treated with HEPES. Class 2 and 4 are HEPES sensitive, indicating they represent KNR-like events (n = 14 cells per condition; t-test followed by Benjamini-Hochberg correction). **F)** Schematic of region of exocytic event (black) and surrounding border pixels (blue). Plots of border pixel $\Delta F/F$ over time demonstrate an event with fluorescence spreading (top, FVF), and an event without (bottom). **G)** Class means +/- SEM of $\Delta F/F$ in pixels surrounding exocytic events. **H)** Half-life of fluorescence decay in pixels surrounding FVFi or FVFd events (border pixels) is not different from the half-life of the exocytic event (center pixels) (n = 14 cells per condition; t-test).

Figure 4

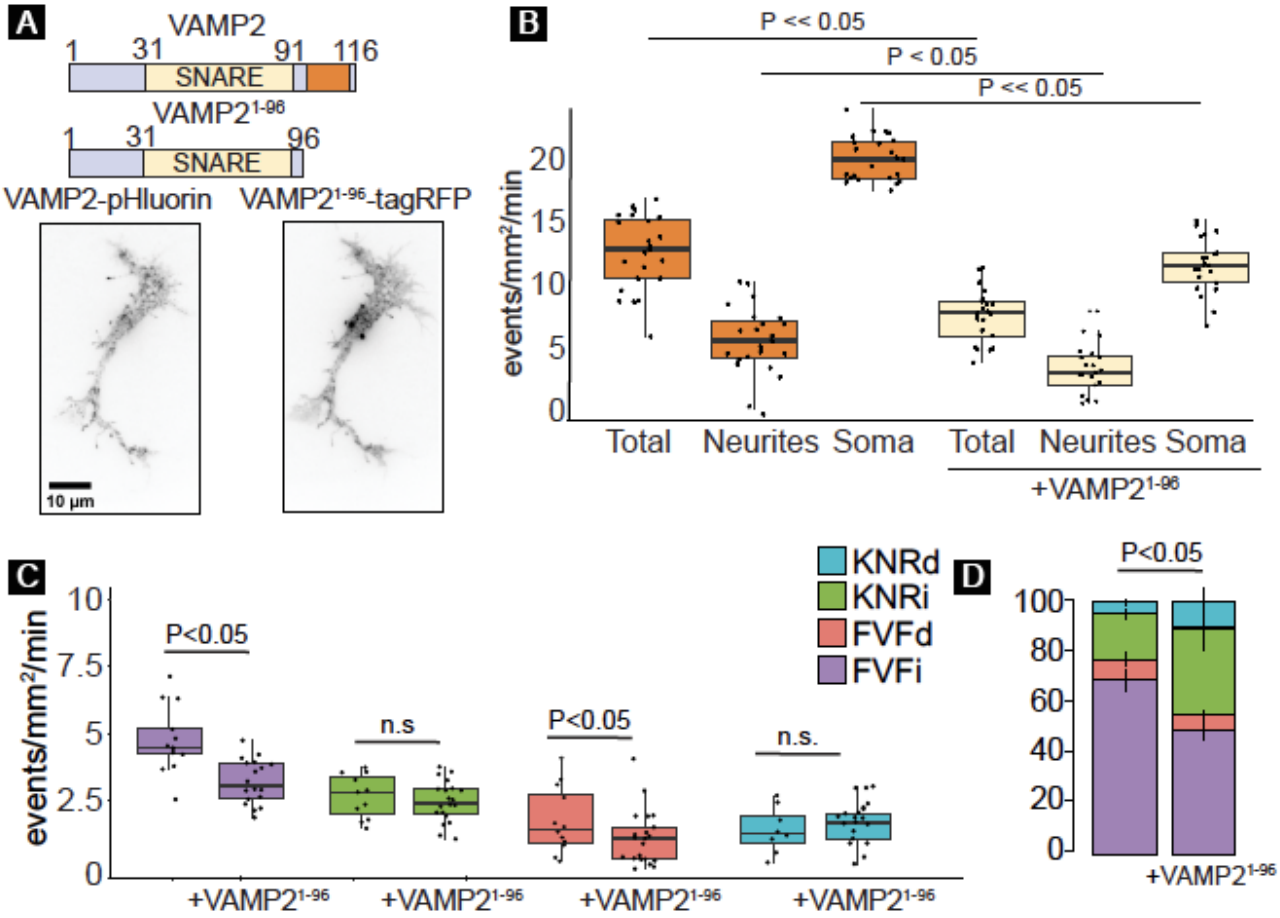

Figure 4: Expression of truncated VAMP2 alters exocytic mode. A) VAMP2-pHluorin and VAMP2$^{1-96}$-tagRFP constructs and representative images of a neuron expressing both of VAMP2-pHluorin and VAMP2$^{1-96}$-tagRFP. **B)** Frequency of exocytic events in the whole cell, soma, and neurites of neurons expressing VAMP2-pHluorin +/- VAMP2$^{1-96}$-tagRFP (n = 23 cells per condition; t-test followed by Benjamini-Hochberg correction). **C)** Frequency of exocytic events of each class of in whole neurons expressing VAMP2-pHluorin +/- VAMP2$^{1-96}$-tagRFP (n = 17 cells per condition; t-test followed by Benjamini Hochberg correction). **D)** Relative proportions of each class of exocytosis in whole neurons expressing VAMP2-pHluorin +/- VAMP2$^{1-96}$-tagRFP (n = 17 cells per condition; multivariate linear regression).

Figure 5

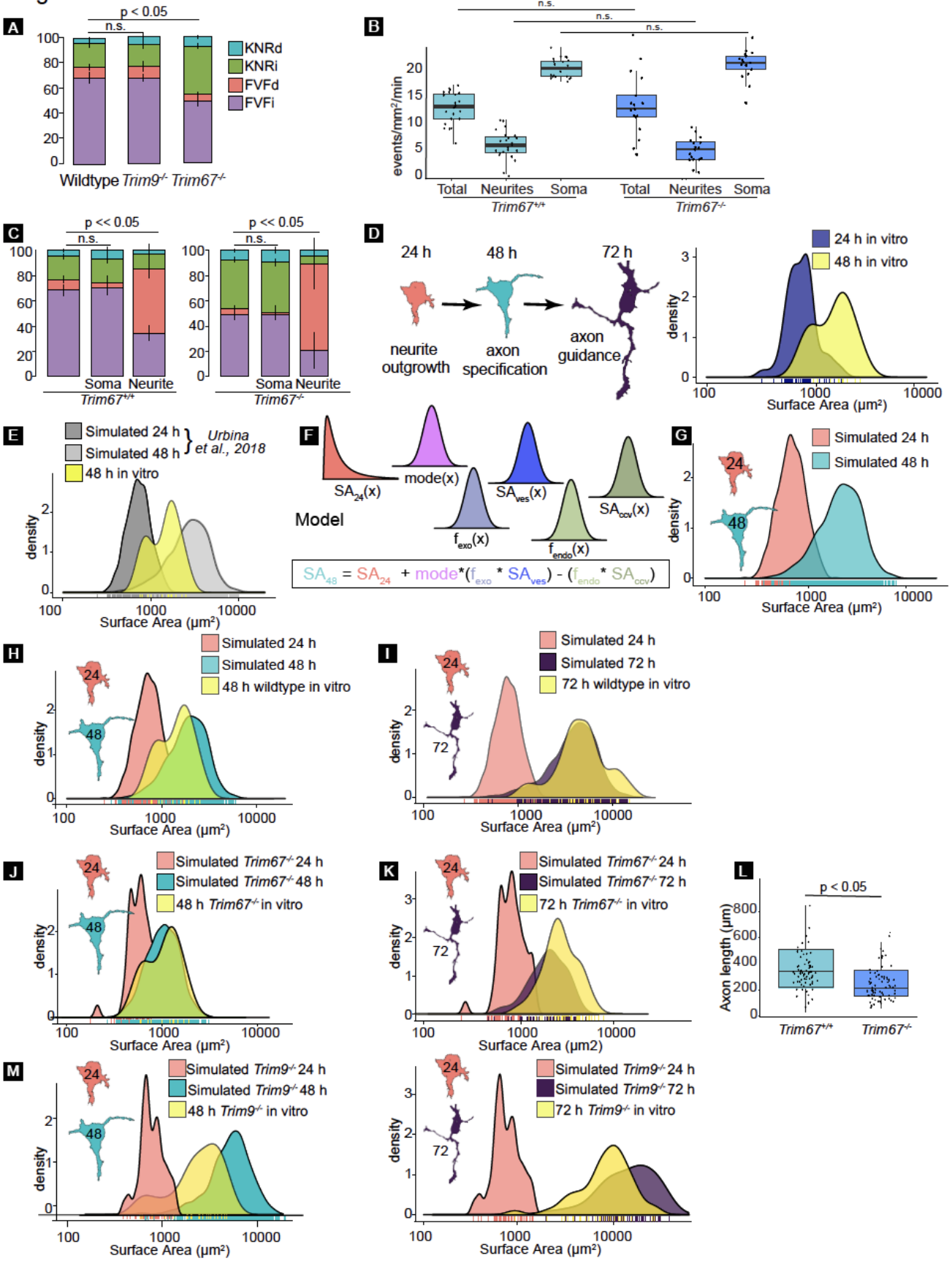

$$SA_{48} = SA_{24} + mode*(f_{exo} * SA_{ves}) - (f_{endo} * SA_{ccv})$$

Figure 5: TRIM67 biases exocytic mode towards full-vesicle fusion. A) Proportion of KNRd, KNRi, FVFd, and FVFi in wildtype, *Trim9*$^{-/-}$, or *Trim67*$^{-/-}$ neurons (n = 15 neurons per condition, multivariate linear regression). **B)** Frequency of exocytic events in the whole neuron, soma, and neurites of *Trim67*$^{+/+}$ or *Trim67*$^{-/-}$ neurons (n = 15 neurons per condition; t-test followed by Benjamini Hochberg correction). **C)** Proportion of KNRd, KNRi, FVFd, and FVFi VAMP2-pHluorin exocytic events in the whole neuron, soma, and neurites of *Trim67*$^{+/+}$ or *Trim67*$^{-/-}$ neurons (n = 15 neurons per condition; multivariate linear regression). **D)** Schematic of neuronal morphogenesis in vitro and empirically measured surface areas from GFP-CAAX expressing wildtype neurons at indicated time points. Surface area calculations were performed as described in (Urbina et al., 2018). **E)** Simulated 24 and 48 hour neurons using the model from (Urbina et al., 2018) that considers all exocytic events FVF. Empirically measured surface area of cortical neurons *in vitro* plotted in yellow. **F)** Overview of new cell model that includes the mode of exocytosis for simulating cell growth. Surface area at 48 hours (SA_{48}) was estimated by first generating a population of neurons at 24 hours (SA_{24}) based on empirical measurements of neurons at 24 hours. The distribution of modes (mode), frequency of exocytosis (f_{exo}), surface area of vesicles (SA_{ves}), frequency of endocytosis (f_{endo}), and surface area of clathrin-coated vesicles (SA_{ccv}) were incorporated into estimating the surface area expansion. **G)** Simulated neuronal surface areas at 24 and 48 h. Surface areas at 24 h are simulated based on empirical measurements of surface area at that time point. Surface areas at 48 h use the 24 h simulation and model described in F. **H)** Simulated surface areas from G, with empirically measured surface areas at 48 h overlaid in yellow demonstrate a better fit that the model that only considers FVF in E. **I)** Simulated neurons at 72 h (purple) with measured surface area at 72 h of neurons *in vitro* overlaid in yellow. **J)** Predicted plasma membrane growth simulated over 24 h using the relative proportion of modes from *Trim67*$^{-/-}$ neurons with empirically measured *Trim67*$^{-/-}$ neurons overlaid in yellow. **K)** Plasma membrane growth of *Trim67*$^{-/-}$ neurons simulated at 72 h, compared to empirically measured neurons (yellow overlay). **L)** Axon lengths of 120 hr *Trim67*$^{+/+}$ or *Trim67*$^{-/-}$ cortical neurons (n = 75, t-test). **M)** Simulations of plasma membrane growth at 48 and 72 h using the distribution of frequencies from *Trim9*$^{-/-}$ cortical neurons as compared to empirically measured *Trim9*$^{-/-}$ neurons (yellow overlay).

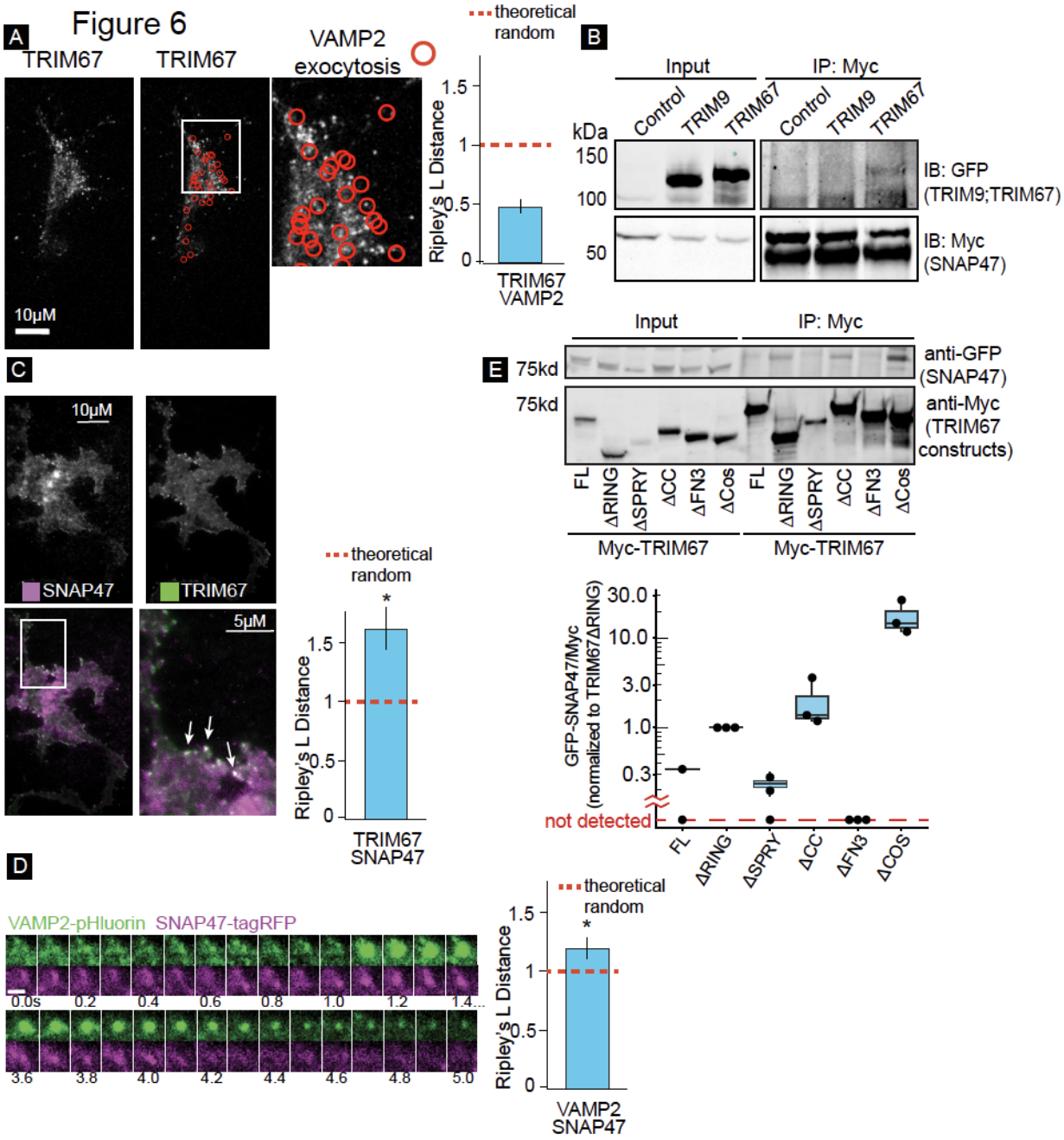

Figure 6: The t-SNARE SNAP47 interacts with TRIM67 and localizes to VAMP2-mediated exocytic events. A) Representative images and Ripley's L Distance co-localization analysis of TRIM67-tagRFP and spatial location of VAMP2-pHluorin events (red circles), demonstrating lack of colocalization (n = 15 cells; value lower than theoretical random suggest not significantly colocalized; analysis described in methods). **B)** Immunoprecipitation of Myc-SNAP47 from HEK293 cells expressing either Myc-SNAP47 and GFP-TRIM67 or Myc-SNAP47 and GFP-TRIM9, blotted for GFP and Myc. GFP-TRIM67 co-immunoprecipitated with Myc-SNAP47 while GFP-TRIM9 was not detectable in the Myc- immunoprecipites. **C)** Representative images and co-localization analysis of SNAP47-tagRFP and TRIM67-GFP in cortical neurons at 48 hours *in vitro* (n = 14 cells; value above theoretical line are significantly colocalized (*); analysis described in methods). **D)** Example of VAMP2-pHluorin and SNAP47-tagRFP co-localization during an exocytic event over time (n = 16 cells; value above theoretical line are significantly colocalized (*);analysis as described in methods) (Scale bar = 1μm). **E)** Structure-function co-immunoprecipitation assays. MycTRIM67 constructs immunoprecipitates blotted for GFP-SNAP47 and Myc. Graph represents relative GFP-SNAP47/Myc-TRIM67 constructs normalized to Myc-TRIM67ΔRING; blots with without a detectable band of GFP-SNAP47 represented below graph break.

Figure 7

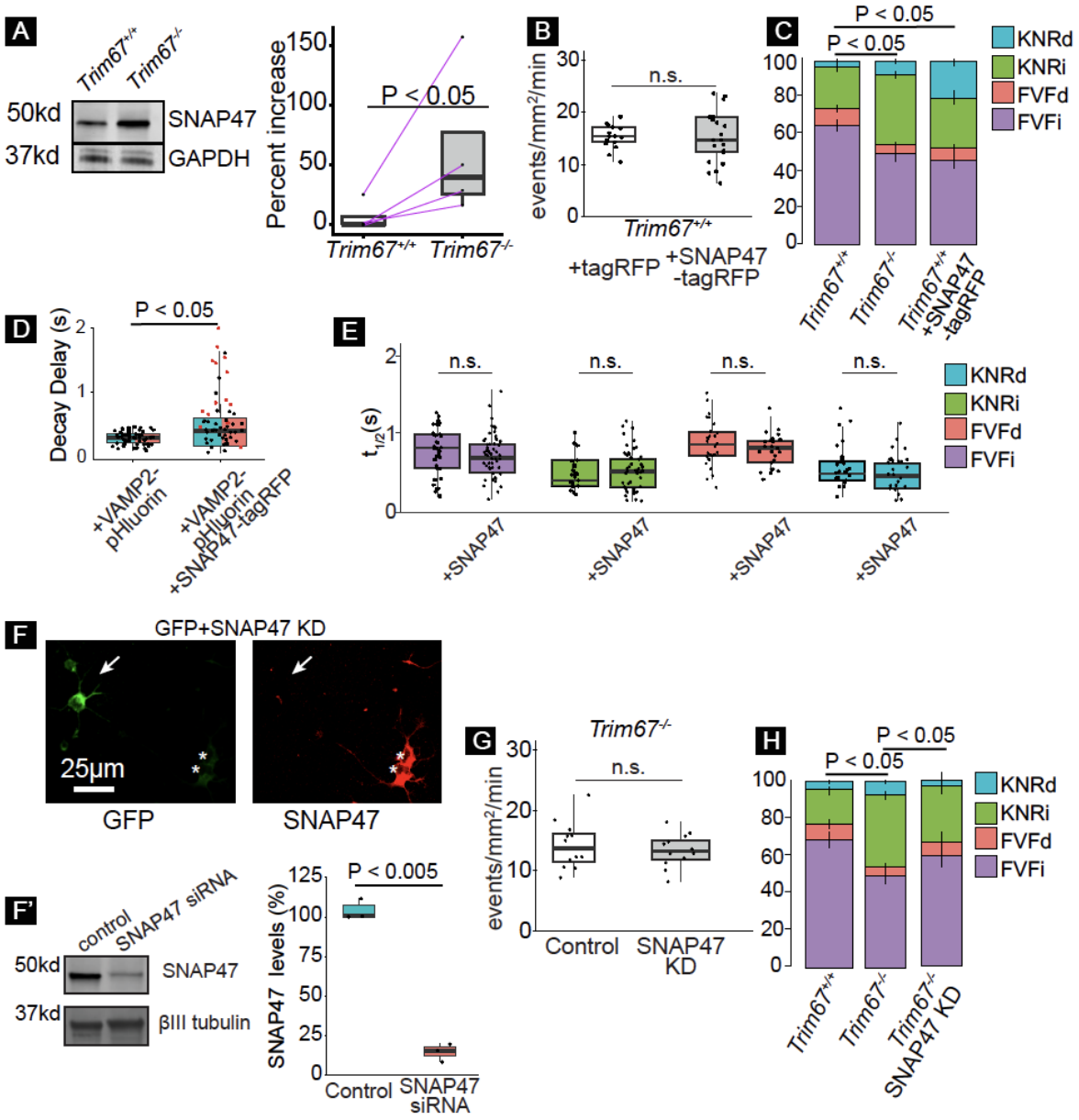

Figure 7: TRIM67 alters exocytosis by modulating SNAP47 protein levels. A) Immunoblot of SNAP47 and GAPDH from total lysate of *Trim67*$^{+/+}$ and *Trim67*$^{-/-}$ cortical neurons at 48 hours *in vitro*. Quantification of percent increase of SNAP47/GAPDH quantified from 4 blots (right; log paired-t-test, analysis in methods). **B)** Frequency of VAMP2-pHluorin exocytosis +/- tagRFP or SNAP47-tagRFP is not significantly differently (n = 16 neurons per condition, t-test). **C)** Relative proportions of exocytic modes in *Trim67*$^{+/+}$ neurons, *Trim67*$^{-/-}$ neurons, or *Trim67*$^{+/+}$ neurons expressing SNAP47-tagRFP (n = 16 neurons per condition; multivariate linear regression). **D)** Quantification of time after peak ΔF/F before fluorescence decay onset of KNRd and FVFd events (n = 17 neurons; t-test). The decay was estimated by fitting sequential exponential decay curves and measuring the time difference between the start of the first and second exponential decay curve fits. **E)** Half-life of each exocytic class +/- SNAP47-tagRFP was not different (n = 17 neurons per condition; t-test with Benjamini-Hochberg correction). **F)** Example SNAP47 immunocytochemistry images in neurons expressing siRNA for SNAP47 knockdown (KD)

(GFP+, arrow), or without (*). Cells were transfected with an eGFP expression plasmid and SNAP47 siRNA followed by immunostaining of SNAP47; GFP positive neurons did not stain for SNAP47, suggesting knockdown of SNAP47. **F')** Immunoblot and quantification of SNAP47 and Beta-III tubulin protein levels in SNAP47 knockdown compared to control (n = 3 experiments; t-test). **G)** Frequency of VAMP2-pHluorin exocytosis +/- SNAP47 siRNA is not different (n = 12 neurons per condition; t-test). **H)** Relative proportions of each exocytic class in *Trim67*$^{+/+}$ neurons, *Trim67*$^{-/-}$ neurons, or *Trim67*$^{-/-}$ neurons with SNAP47 knockdown (n = 12 neurons per condition, multivariate linear regression).

Figure 8

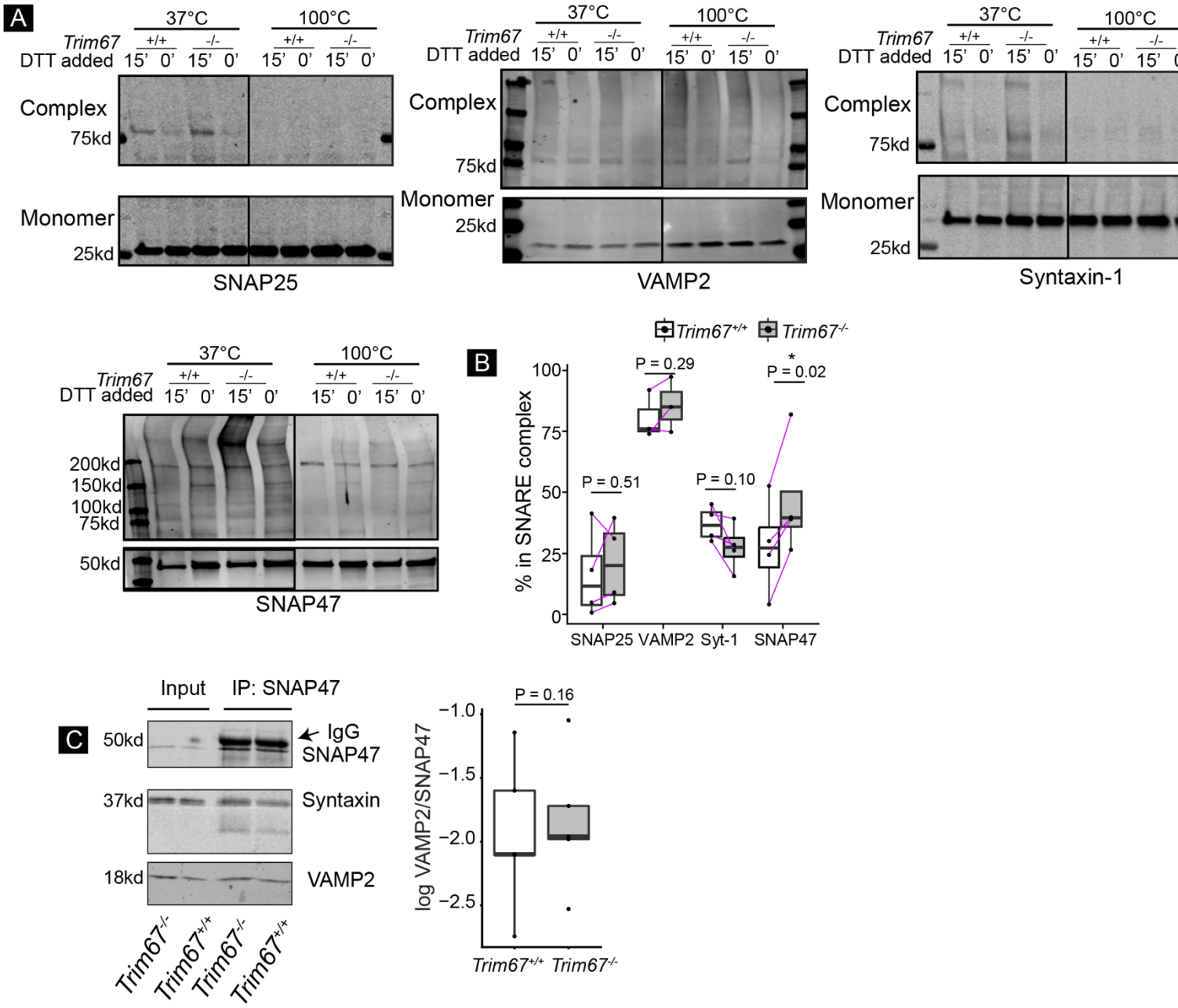

Figure 8: TRIM67 reduces SNAP47 incorporation into SNARE complexes. A) Immunoblot of monomeric and high molecular weight SNARE proteins, interpreted as SNARE complexes. Cortical neurons were treated with NEM (15 minutes) to preserve SNARE complexes followed by DTT (15 minutes) to quench NEM, or NEM+DTT as a negative control (30 minutes). Samples were lysed and split into two aliquots, one incubated at 100ºC to disassociate SNARE complexes and one at 37ºC (control). Increased intensity of bands above 37kD (50kD for SNAP47) in the presence of NEM-only at 37ºC suggest formed SNARE complexes. **B)** Quantification of % SNARE proteins in SNARE complexes (intensity of lane above 37kD or 50kD/(monomer + intensity of lane; n = 4 blots, log-ratio paired t-test; see methods)). **C)** Immunoprecipitation of endogenous SNAP47 in neuronal membrane fractions at 48 hours *in vitro* immunoblotted for SNAP47, syntaxin-1, and VAMP2.

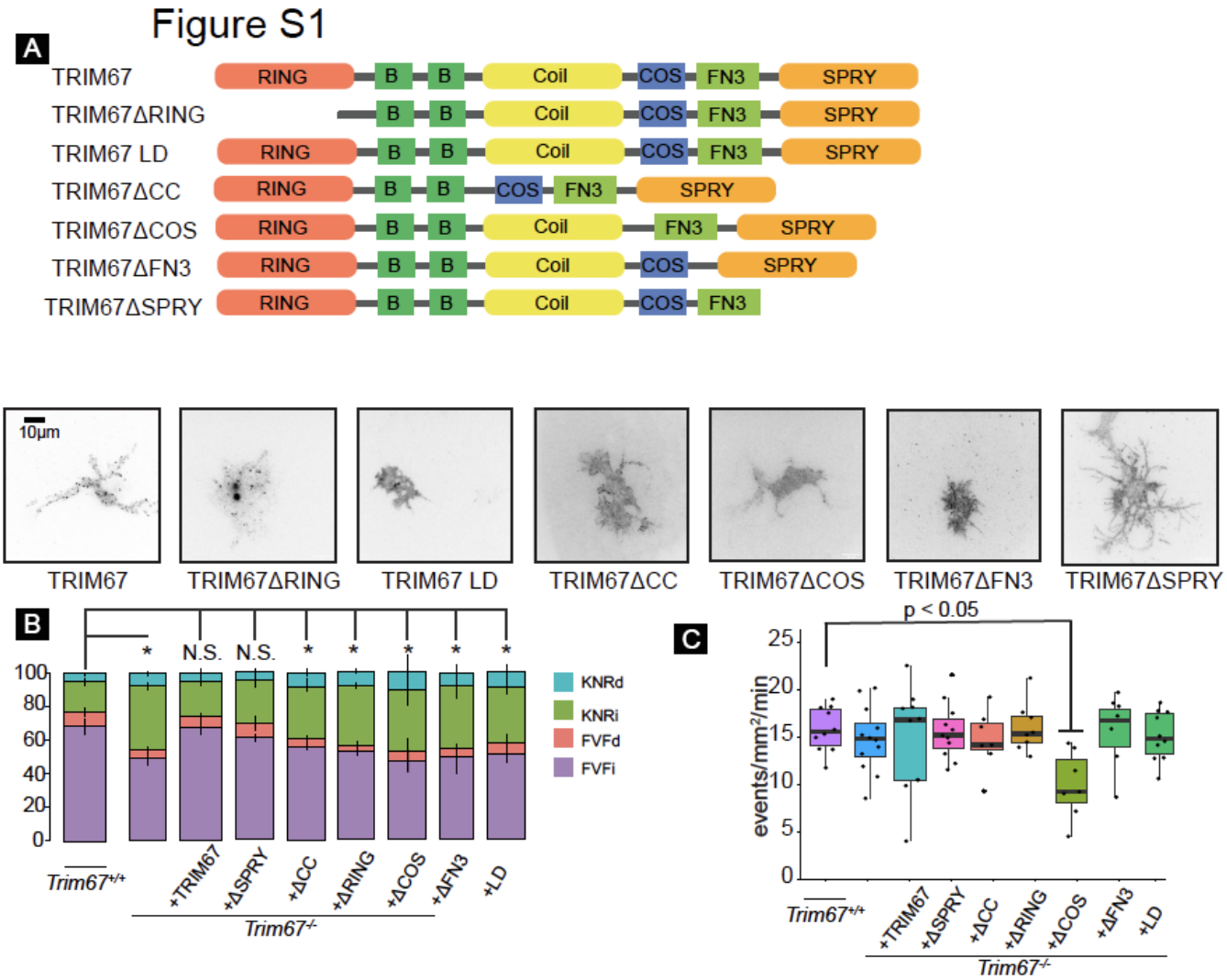

Figure S1: Multiple domains of TRIM67 and ligase function are required for exocytic mode regulation. A) Domain architecture of TRIM67 constructs tagged with TagRFP for structure:function assays. Example fluorescence images of each mutant (below). **B)** Relative proportion of each exocytic class (multivariate linear regression) and **C)** exocytic frequency in *Trim67*$^{+/+}$ neurons, *Trim67*$^{-/-}$ neurons, or *Trim67*$^{-/-}$ neurons expressing VAMP2-pHluorin and TRIM67-tagRFP constructs (n = 14 cells per condition; t-test with Benjamini-Hochberg correction).

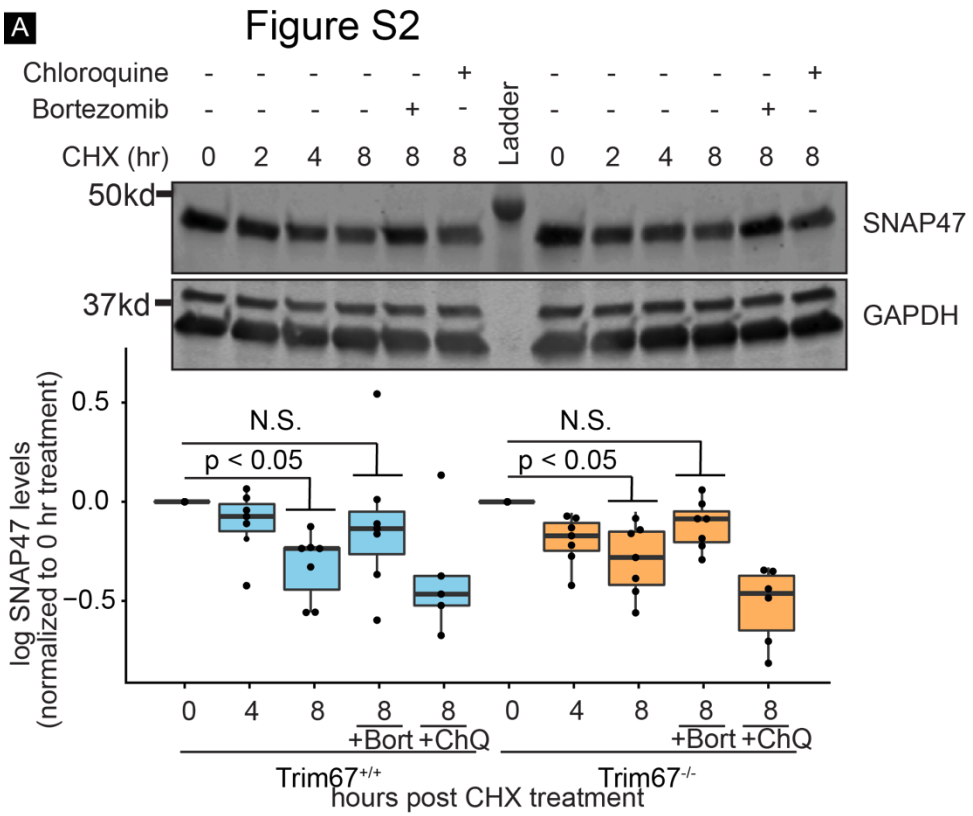
A
Figure S2
Chloroquine
Bortezomib
CHX (hr)
Ladder
50kd
37kd
SNAP47
GAPDH
log SNAP47 levels
(normalized to 0 hr treatment)
N.S.
p < 0.05
+Bort
+ChQ
Trim67+/+
Trim67-/-
hours post CHX treatment

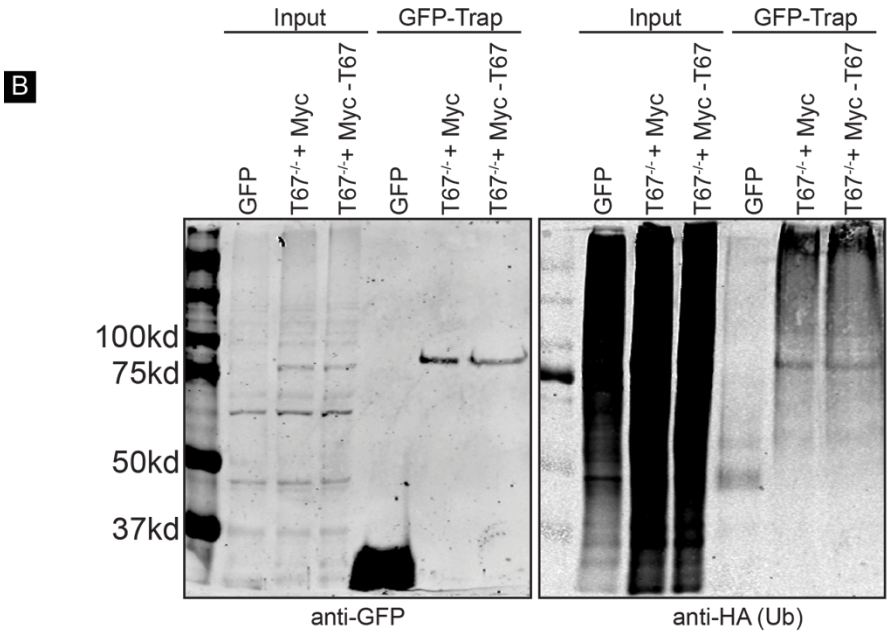
B
Input
GFP-Trap
GFP
T67-/- + Myc
T67-/- + Myc -T67
100kd
75kd
50kd
37kd
anti-GFP
anti-HA (Ub)

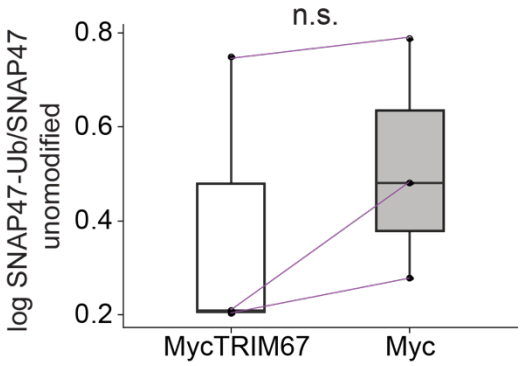
n.s.
log SNAP47-Ub/SNAP47
unomodified
MycTRIM67
Myc

Figure S2: Proteasomal degradation and ubiquitination of SNAP47 are TRIM67 independent. A) Immunoblot of neuronal lysates at 48 hrs after treatment with cycloheximide (CHX,50 µg/µl) for 0, 2, 4, 8 hrs or cycloheximide (50 µg/µl) +/- bortezomib (Bort) (200 nM) for 8 hrs or cyclohexamine(50 µg/µl) +/- chloroquine (ChQ) for 8 hours (log-ratio paired t-test (methods) performed between genotypes at each timepoint followed by Benjamini-Hochberg correction; n = 7 blots, n =5 for CHX+ChQ in *Trim67*$^{+/+}$, n =6 for CHX+ChQ in *Trim67*$^{-/-}$). **B)** Immunoblot of lysates and immunoprecipitation in *TRIM67*$^{-/-}$ HEK cells expressing HA- tagged ubiquitin (HA-Ub) along with empty GFP or GFP-tagged SNAP47 (GFP-SNAP47) with empty-Myc or Myc-tagged TRIM67 (Myc-TRIM67). Cells overexpressing these constructs were treated with MG132 for 4 hrs prior to lysis to prevent proteosomal degradation (log-ratio paired t-test (methods), n = 3).

Methods

Plasmids and antibodies

Plasmid encoding human-VAMP2-pHluorin was acquired from James Rothman (Yale, New Haven, CT). VAMP2-tagRFP was created by PCR of VAMP2 of VAMP2-pHluorin and cloning into the tagRFP vector. VAMP21-96-tagRFP was created by partial PCR of VAMP2 (AA 1-96) followed by cloning into a tagRFP vector. Myc-SNAP47 was obtained from Thierry Galli (University of Paris, France). SNAP47-tagRFP was cloned created by PCR of SNAP47 from Myc-SNAP47 followed by cloning into a tagRFP vector. TRIM67 constructs were made as described in (Boyer et al., 2020). Flag-tagged Ubiquitin was obtained from Ben Philpot (University of North Carolina at Chapel Hill, Chapel Hill, NC). GFP-CAAX was obtained from Richard Cheney (University of North Carolina at Chapel Hill, Chapel Hill, NC). Antibodies included rabbit polyclonal against TRIM67 (Boyer et al., 2018); mouse monoclonal against TRIM9 (H00114088-M01, Abnova); mouse monoclonal against c-Myc (9E10); mouse monoclonal against human β-III-tubulin (TujI SCBT); ubiquitin (sc-8017, SCBT); GAPDH (sc-166545, SCBT); GFP-Trap® Agarose (Chromotek); VAMP2 (D6O1A) Rabbit mAb #13508 (Cell Signaling); Syntaxin-1 (sc-12736, Santa Cruz); SNAP25, Mouse monoclonal (Synaptic Systems); HA, from the lab of Patrick Brennwald (UNC: Chapel Hill); IRDye® 800CW Donkey anti-Mouse IgG Secondary Antibody and IRDye® 680LT Goat anti-mouse Secondary Antibody (Licor); rabbit polyclonal against HA (71-5500, Thermo Fisher Scientific); siRNAs pool targeting SNAP47 were purchased from Dharmacon (target sequence 5'- CGTACGCGGAATACTTCGA-3').

Animal Work

All mouse lines were on a C57BL/6J background and bred at UNC with approval from the Institutional Animal Care and Use Committee. Mouse colonies were maintained in specific pathogen-free environment with 12-12 hr light and dark cycles. Timed pregnant females were obtained by placing male and female mice together in a cage overnight; the following day was designated as embryonic day 0.5 (E0.5) if the female had a vaginal plug. *Trim9*$^{-/-}$ mice were described in Winkle et al., 2014 and *Trim67*$^{-/-}$ mice were generated in(Boyer et al., 2018)Mice were genotyped using standard tail genotyping procedures. For all culture experiments, embryos from time-matched homozygous WT, homozygous *Trim9*$^{-/-}$, or homozygous *Trim67*$^{-/-}$ were used.

Media, culture and transfection of primary neurons and immortalized cell lines

Both male and female embryos were used to generate cultures and were randomly allocated to experimental groups. Cortical neuron cultures were prepared from day E15.5 embryos as previously described (Viesselmann et al., 2011). Briefly, cortices were micro-dissected and neurons were dissociated with 0.25% trypsin for 15 minutes at 37C followed by quenching with

neurobasal media supplemented with 10% FBS and 0.5 mM glutamine. After quenching, cortices were gently triturated 15x and cells were counted by haemocytometer. Cells were spun at 0.1xg for 7 min at room temperature. After aspiration of the media, pelleted neurons were resuspended in neurobasal media supplemented with B27 (1:50 of manufacturer stock (Invitrogen)) and plated on cover glass or tissue culture plastic coated with 1 mg/ml poly-D-lysine (Sigma-Aldrich).To assay axon length, and plated on poly-D-lysine coated glass-bottom culture dishes in neurobasal media supplemented with B27 (Invitrogen). This same media was used for all time-lapse experiments. For transfection, neurons were resuspended after dissociation in solution (Amaxa Nucleofector; Lonza) and electroporated with a nucleofector according to manufacturer's protocol. For transfection of plasmids and siRNA, neurons were resuspended after disassociation in Lonza Nucleofector solution (VPG-1001) and electroporated with Amaxa Nucleofector according to manufacturer protocol or transfected with Polyplus jetPRIME® reagent as per manufacturer's protocol. HEK cells were transfected with Lipfectamine 2000 (Invitrogen) according to manufacturer protocol. HEK293 cells (female) were obtained fom Rothenfußer (Klinikum der Universit¨at München, München, Germany). *Trim67*$^{-/-}$ HEK293 cells were generated from this line by CRISPR/Cas9 editing as described in (Boyer et al., 2020). HEK293 cells were maintained at 5% CO2 at 37C in DMEM with glutamine (Invitrogen) supplemented with 10% FBS (Hyclone).

HEPES, TeNT, cycloheximide, bortezomib, and chloroquine treatments

For these assays, neurons were transfected with VAMP2-pHluorin and imaged at 48 hours. Neurons were imaged as described in "Live imaging and image analysis". For TeNT experiments, 50 nM of TeNT (Sigma) were added to the neurons followed by imaging 30 minutes after the addition of TeNT. For HEPES experiments, exocytic events were imaged immediately after addition of 60mM of HEPES to the imaging media. For treatment with cycloheximide,bortezomib, or chloroquine, prior to lysis the cells were treated with cycloheximide (50 µg/µl) for 0, 2, 4, 8 hrs or cycloheximide (50 µg/µl) and bortezomib (200 nM) for 8 hrs or cycloheximide (50 µg/µl) and chloroquine (50 µM) for 8 hrs.

SNAP47 siRNA knockdown

siRNA experiments – a pool of 4 siRNAs targeting mouse SNAP-47 and control Luciferase siRNA (Target Sequence: 5'-CGTACGCGGAATACTTCGA-3') were purchased from Dharmacon (Thermofisher Scientific). Lipofectamine 2000 (Life Technologies) was used as following: GFP or GFP + 50pmol siRNAs were transfected using nucleofection. Cells were fixed and immunostained at 72 hours.

Live imaging

All time-lapse imaging was performed using an inverted microscope (IX81-ZDC2) with MetaMorph acquisition software, an Andor electron-multiplying charge-coupled device (iXon), and a live cell imaging chamber (Tokai Hit Stage Top Incubator INUG2-FSX). A UAPON 100x/1.49 NA DIC TIRF objective (Olympus) and a 40x/1.39 NA DIC objective (Olypus) were used for microscopy. The live cell imaging chamber-maintained humidity, temperature at 37°C, and CO_2 at 5%. Fixed cells were imaged at room temperature in glycerol and n-propyl-gallate-based mounting medium.

For all primary neuron exocytosis assays, neurons expressing VAMP2-pHluorin and/or tagRFP expressing constructs were imaged at the indicated timepoint *in vitro* with a 100x 1.49 NA TIRF objective and a solid-state 491-nm laser illumination and a and a solid-state 561-nm laser, both at 35% power at 110-nm penetration depth. Images were acquired using stream acquisition, imaging once every 100ms for 2 minutes with 100 ms exposure time (10 Hz).

For all colocalization experiments and where two different lasers were used in conjunction with each other, a Hamamatsu W-VIEW GEMINI image splitter optic (A12801-01) was used for simultaneous imaging of both lasers by splitting and projecting the beams, by wavelength, side-by-side onto an electron-multiplying charge-coupled devince (iXon).

Image definitions

Border pixels were defined as the fluorescence of the perimeter 15 pixels wide adjacent the segmented gaussian-shaped fluorescent signal at timepoint 1 (segmented as described in(Urbina et al., 2018). For neurite and soma segmentation, the soma was segmented from the neurites as a rough ellipsoid encompassing the body of the neuron. We defined a neurite as an axon if it was at least 2x longer than the second-longest axon. Axon measurements were made using the NeuronJ plugin in ImageJ.

Image analysis

ImageJ software was used for general viewing of images and frames. For analysis, all VAMP2-pHluorin exocytic events were detected using the automated detection software as described (Urbina et al., 2018) in Matlab and R with Rstudio

To determine co-localization, TRIM67tagRFP and SNAP47tagRFP puncta were identified by difference-of-gaussian spot detection. The x,y centroids of VAMP2-pHluorin events, SNAP47-tagRFP puncta, or TRIM67-tagRFP puncta the fit with a marked point process model, and their Ripley's L value distance was measured normalized to the number of puncta and area for each cell (Grantham, 2012). The Ripley's L values were compared to theoretically random marked points, setting a threshold of 0.05% chance to fall below the theoretical Ripley's L value. All values were normalized to the theoretical Ripley's L value for comparisons.

To determine the rate of decay of fluorescence ($t^{1/2}$), we used an exponential decay model for FVFi and KNRi:

$$V(t) = V_0 e^{-\lambda t}$$

To estimate the $t_{1/2}$ (λ), the log of fluorescence from peak ΔF/F until the end of decay were fit to a linear model:

$$ln(V(t)) = -\lambda t$$

In which V(t) is the fluorescence intensity at each timepoint and t is time in seconds.

To estimate the rate of decay of FVFd and KNRd, two sequential exponential decay models were fit. The log of fluorescence from peak ΔF/F until the end of decay were fit using segmented regression, with the breakpoint between the two regressions decided by iteratively moving the breakpoint one time-step, fitting segmented regression, and minimizing the sum of squared error. The breakpoint that has the lowest total error is considered the true breakpoint. The first regression represents the "delay" before decay starts, and second regression's $t_{1/2}$ represents the fluorescence decay.

Plots

All boxplots were graphed as follows: the box represents the median value (middle of boxplot) and the interquartile range, which is the distance between the first and third quartile of the data (with the first quartile being the middle value between smallest number and median of the

dataset, and the third quartile representing the middle value between the largest number and median of the dataset). The whiskers represent 1.5x the interquartile range.

Statistical estimation and modeling of surface area

Surface Area Estimation

To estimate the surface area, we used TIRF images of VAMP2-pHluorin expressing cells. The soma was identified and segmented from the neurites, and the basal surface area of each were calculated separately. Total neurite area was estimated as doubling the measured basal membrane area. The average height of the soma (~11 μm) was obtained from confocal image z stacks through cortical neurons at 48 hours in vitro. The major and minor axis of the soma were measured, and used with the average height of the soma to calculate the surface area using the following calculation for a truncated ellipsoid:

$$\frac{3}{4}4\pi\left(\frac{(ab)^{1.6}+(ac)^{1.6}+(bc)^{1.6}}{3}\right)^{\frac{1}{1.6}}+\frac{\pi ab}{c^2}(0.75c)(3c-0.75c)$$

Where a,b, and c represent the 3 axes of the soma (length, width, and height, respectively). The surface area of soma and neurites were summated to obtain the final surface area estimate of the neuron.

Model Selection

We constructed our Bayesian linear model based off of the model built in the previous paper (Urbina et al., 2018). Surface area, our predicted and independent variable, is a positive, continuous, right skewed distribution, which has a non-uniform standard deviation over time. With this knowledge, we constructed several models, selecting for probability distributions that would fit the criteria of positive, continuous, and right-skewed data: log-normal, Skew-normal, and Gamma. We also constructed models using the t-distribution and the normal distribution as a base model, as these are statistically well-studied and well-characterized distributions. For these priors, we chose loose, non-committal and reasonable ranges for the normal and t-distribution (a mean of 1000 and a standard deviation of 10, which would easily encompass all possible sizes neurons). Using previously published data, we used the estimated posterior probability parameters as the new priors for these experiments. This allowed us to confidently construct priors that were estimated from previously measured neuronal surface area. From this, we constructed 5 hierarchical models: Gamma with a log-link, log-normal, skewed-normal, and log-normal with a lower bound truncation of 0. In addition, given the noted difference in the standard deviation between the observed surface area at 24 hours and at 48 hours, we added in a 5th model, in which the standard deviation was also modeled based on the two time point observations. 4 chains were run with 100,000 samples after a burn-in period of 10,000 steps for a total of 110,000 steps in order to ensure chain convergence and enough coverage of the posterior distribution. Model evaluation using Rhat and ESS suggested the chains were well-mixed and converged properly. Each of these models were then compared by computing Watanabe-Akaike information criteria and using leave-one-out validation to compute the expected log pointwise predictive distribution for the difference in each of the models. Model selection using these criteria indicate that using the log-normal family results in the best fit for these data, followed by the gamma distribution. Taking all of these terms into account, we constructed an equation for the hierarchical Bayesian linear model using the log-normal distribution:

Y ~ N(B0 + B1xi, sigma ~ N(0,1))

Classification

Numerous clustering validity algorithms have been proposed (Rousseeuw, 1987; Pelleg et al., 2000; Sugar and James, 2003). These algorithms combine information about intracluster compactness and intercluster isolation, as well as other factors, such as geometric or statistical properties of the data, the number of data objects, and the dissimilarity or similarity measurements. However, different algorithms lead to different clusters, and even in a single algorithm, choice of parameters can lead to different clusters. To perform classification, we used a majority-rules decision of 20 well-used algorithms for determining cluster, including the silhouette method and elbow method.Each of the four classification datasets (feature extraction, Euclidean distance, and DTW distance) were clustered into four classes based on minimizing within-cluster sum of squares.

Statistical analysis

The software package R was primarily used for statistical analysis of data. Both R and Adobe Illustrator were used for the generation of figures. At least three independent experiments were performed for each assay. For two-sample comparisons of normally distributed data, Welch's t-test was used for two independent samples, or paired t-test for paired samples. For multiple comparisons, Welch's or paired t-tests corrected using Benjamini-Hochberg method. For comparison of ratios for the four classes, multivariate linear regression was used, with the expected ratio of the four classes as the dependent variables and the conditions as the independent variables. For analysis of Fig 1G, a chi-squared expected ratio test was performed to determine if the pHluorin classification assigned FVF or KNR classes different than randomly. For analysis of non-normally distributed data, the was used to determine significance followed by the method described above.

Western blot analysis

Unless indicated differently, all western blot samples were resolved by SDS-PAGE followed by transfer onto 0.45μM (0.22μM for the SNARE complex assay) nitrocellulose paper and analyzed by immunoblotting. Blots were probed with indicated primary antibodies, followed by IRDye® 680LT Goat anti-Rabbit Secondary Antibody and/or IRDye® 800CW Donkey anti-Mouse IgG Secondary Antibody and imaged on an Odyssey Licor. Unless indicated differently, all western blot comparisons, the relative intensity or relative ratios were log-transformed followed by paired-t-test between the log-transformed data. Western blots were analyzed using Fiji (ImageJ), with total fluorescence of labeled bands representing relative protein normalized to control conditions for each experiment as indicated.

SNARE complex assay

SNARE complexes were performed as described in (Hayashi et al., 1994) with modifcation. E15.5 cortical neurons at 48 hours *in vitro* were treated with either NEM (15 minutes) or NEM+DTT (15 minutes) prior to lysis in homogenization buffer containing 20mM HEPES-NaOH, 320mM sucrose, and protease inhibitors. Lysates were homogenized in a homogenization buffer (10mM HEPES-NaOH, pH 7.4, 150mM NaCl, 1mM EGTA, 1mM NEM, and protease inhibitors). Tx-100 was added to lysates to make a final composition of 1% Tx-100. Lysates were triturated 10x and solubilized for 2 min on ice then centrifuged at 10min, 6000 xg. Samples were diluted in 4x sample buffer (200mM Tris-Cl, pH 6.8, 8% SDS, 0.4% Bromophenol Blue, 40% glycerol, 20% 2-Mercaptoethanol) into two replicates, one replicate incubated at 100 °C for 10 min and the second incubated at 37 °C for 10 min.

Co-immunoprecipitation assay

For coimmunoprecipitation assays to investigate SNAP47 interaction with TRIM67, HEK cells were transfected with plasmids expressing MycTRIM9 or MycTRIM67 full length constructs or TRIM67 domain deletion mutants along with a GFP-tagged SNAP47 construct using Polyplus jetPRIME® reagent as per manufacturer's protocol. The cells were lysed using the immunoprecipitation (IP) buffer (10% glycerol, 1% NP-40, 50 mM Tris pH 7.5, 200 mM NaCl, 2 mM $MgCl_2$ and protease and phosphatase inhibitors). Cells were scraped from the dish and transferred into tubes, then centrifuged at 14,000 rpm for 10 min. Approximately 500–1,000 µg of protein per sample was used per IP. Myc-tagged proteins were bound using a homemade monoclonal anti-Myc antibody (9E10) incubated overnight followed by Protein A coupled agarose beads. Beads were washed twice with IP buffer and then boiled with 2X sample buffer. For endogenous SNAP47 immunoprecipitation, membrane proteins were enriched through ultra-centrifugation of neuronal lysates, as described in (Shimojo et al., 2015). Briefly, cortices of wild-type mice were homogenized in 20 mM HEPES-NaOH (pH 7.4), 320 mM sucrose, 5 µg/ml leupeptin, 2 µg/ml aprotinin, and 1 µg/ml pepstatin. Membrane fractions were isolated by two sequential steps of centrifugation at 3,000 and 100,000 × g and solubilized for 30 min in 20 mM HEPES-NaOH (pH 7.4), 150 mM NaCl, and 1% Triton X-100. Protein extracts were cleared by centrifugation at 100,000 × g and incubated overnight with sepharose beads (Sigma) coated with -SNAP47, or control IgG antibodies (Sigma). Attached complexes were then washed five times with extraction buffer, eluted from the beads with an SDS gel loading buffer, and resolved by SDS-PAGE.

Ubiquitination experiment

For the ubiquitination assay we expressed HA- tagged ubiquitin (HA-Ub) along with empty GFP or GFP-tagged SNAP47 (GFP-SNAP47) with an empty Myc or Myc-tagged TRIM67 (Myc-TRIM67) in *TRIM67*$^{-/-}$ HEK cells(transfected using Lipofectamine 2000). GFP-Trap beads (Chromotek) were used to enrich GFP-SNAP47 and GFP according to manufacturer protocol. Briefly, cells were treated with MG132 for 4 hrs then lysed in ubiquitination immunoprecipitation (IP) buffer (50 mM Tris-Cl, 150 mM NaCl, 1 mM EDTA, 0.5% Triton X, 0.7% *N*-ethylmaleimide, and protease and phosphatase inhibitors, pH 7.3–7.4). Cells were scraped from the dish and transferred into tubes, then centrifuged at 14,000 rpm for 10 min. Approximately 500–1,000 µg of protein per sample were used in each assay. 15 µl GFP-TRAP beads were incubated with the lysate for 2.5 hrs followed by three washes. The first wash was performed using 10mM Tris-Cl, pH7.5, 150 mM NaCl, 0.5 mM EDTA, 0.7% NEM. This was followed by two washes using first a stringent buffer (8 M Urea, 1% SDS) and then SDS wash buffer (1% SDS). The beads were then boiled with 2X sample buffer.

Protein half-life experiment

For protein half-life measurements, embryonic cortical neurons from E15.5 wildtype or *Trim67*$^{-/-}$ pups were dissociated and plated on PDL-coated dishes. The cells were lysed at 48 hrs (2 DIV). Prior to lysis the cells were treated with cycloheximide (50 µg/µl) for 0, 2, 4, 8 hrs or cycloheximide (50 µg/µl) and bortezomib (200 nM) for 8 hrs. The cells were lysed with lysis buffer (300 mM sucrose, 1% NP-40, 50 mM Tris pH 7.5, 200 mM NaCl, 2 mM $MgCl_2$ and protease, phosphatase and deubiquitinase inhibitors*)*. Protein concentrations were estimated, and the lysates were boiled with 2x sample buffer and resolved by western blot.

Mass Spectrometry

To identify potential interacting partners for TRIM67 we used the Proximity-Dependent Biotin Identification (BioID) approach (Roux et al. JCB 2012). Full details are results are in preparation (Menon et al.,). Briefly, the negative control Myc-BirA* and Myc-BirA* TRIM67ΔRING was packaged into Short Term Herpes Simplex Virus (HSV)(MGH) and driven under a IE 4/5 promoter. GFP expression is driven in tandem downstream of a mCMV promoter. Cortical neurons from wildtype and *Trim67*$^{-/-}$ E15.5 litters that were dissociated and plated on PDL coated tissue culture dishes. Approximately 40 hours post-plating the neurons were transfected with HSV (MOI = 1.0) carrying either the negative control Myc-BirA* or Myc- BirA* TRIM67ΔRING. 6 hrs post-infection neurons were treated with 50 μM Biotin for 24 hrs. After incubation the cells were lysed using RIPA buffer (150 mM NaCl, 25 mM Tris-HCl, pH 7.5, 0.1% SDS, 1.0% NP-40, 0.25% Deoxycholic acid, 2 mM EDTA, 10% glycerol, protease and phosphatase inhibitors). Biotinylated proteins were then enriched using Streptavidin-conjugated Sepharose beads. The enriched proteins were trypsinized and eluted using the RapiGEST SF Surfactant protocol (Waters). C18 column and Ethyl acetate extraction protocols were employed to prepare the peptides for mass spectrometry. The peptides identified from 3 different replicates were sorted based on their Bayesian False Discovery Rate values.

Acknowledgements

The authors would like to thank Shawn Gomez for critical comments on dynamic time warping, Caroline Monkiewicz, Vong Thoong, and Chris Hardie for mouse breeding, husbandry, and genotyping. Funding from the National Institutes of Health supported this research: including R01NS112326 (SLG), R35GM135160 (SLG), and F31NS103586 (FLU).

References

Alabi, A.A., and R.W. Tsien. 2013. Perspectives on Kiss-and-Run: Role in Exocytosis, Endocytosis, and Neurotransmission. *Annu. Rev. Physiol.* 75:393–422. doi:10.1146/annurev-physiol-020911-153305.

Albillos, A., G. Dernick, H. Horstmann, W. Almers, G.A. de Toledo, and M. Lindau. 1997. The exocytotic event in chromaffin cells revealed by patch amperometry. *Nature*. 389:509–512. doi:10.1038/39081.

Aoki, R., T. Kitaguchi, M. Oya, Y. Yanagihara, M. Sato, A. Miyawaki, and T. Tsuboi. 2010. Duration of fusion pore opening and the amount of hormone released are regulated by myosin II during kiss-and-run exocytosis. *Biochem. J.* 429:497–504. doi:10.1042/BJ20091839.

Archer, D.A., M.E. Graham, and R.D. Burgoyne. 2002. Complexin Regulates the Closure of the Fusion Pore during Regulated Vesicle Exocytosis. *J. Biol. Chem.* 277:18249–18252. doi:10.1074/jbc.C200166200.

Bao, H., D. Das, N.A. Courtney, Y. Jiang, J.S. Briguglio, X. Lou, D. Roston, Q. Cui, B. Chanda, and E.R. Chapman. 2018. Dynamics and number of trans-SNARE complexes determine nascent fusion pore properties. *Nature*. 554:260–263. doi:10.1038/nature25481.

Bello, O.D., S.M. Auclair, J.E. Rothman, and S.S. Krishnakumar. 2016. Using ApoE Nanolipoprotein Particles To Analyze SNARE-Induced Fusion Pores. *Langmuir*. 32:3015–3023. doi:10.1021/acs.langmuir.6b00245.

Bowser, D.N., and B.S. Khakh. 2007. Two forms of single-vesicle astrocyte exocytosis imaged with total internal reflection fluorescence microscopy. *Proc. Natl. Acad. Sci.* 104:4212–

4217. doi:10.1073/pnas.0607625104.

Boyer, N.P., L.E. McCormick, S. Menon, F.L. Urbina, and S.L. Gupton. 2020. A pair of E3 ubiquitin ligases compete to regulate filopodial dynamics and axon guidance. *J. Cell Biol.* 219. doi:10.1083/jcb.201902088.

Boyer, N.P., C. Monkiewicz, S. Menon, S.S. Moy, and S.L. Gupton. 2018. Mammalian TRIM67 Functions in Brain Development and Behavior. *eneuro*. 5:ENEURO.0186-18.2018. doi:10.1523/ENEURO.0186-18.2018.

Bretou, M., O. Jouannot, I. Fanget, P. Pierobon, N. Larochette, P. Gestraud, M. Guillon, V. Emiliani, S. Gasman, C. Desnos, A.-M. Lennon-Duménil, and F. Darchen. 2014. Cdc42 controls the dilation of the exocytotic fusion pore by regulating membrane tension. 25. doi:10.1091/mbc.E14-07-1229.

Burri, L., and T. Lithgow. 2004. A Complete Set of SNAREs in Yeast. *Traffic*. 5:45–52. doi:10.1046/j.1600-0854.2003.00151.x.

Charrad, M., N. Ghazzali, V. Boiteau, and A. Niknafs. 2014. **NbClust** : An *R* Package for Determining the Relevant Number of Clusters in a Data Set. *J. Stat. Softw.* 61:1–36. doi:10.18637/jss.v061.i06.

Chernomordik, L. V., and M.M. Kozlov. 2008. Mechanics of membrane fusion. *Nat. Struct. Mol. Biol.* 15:675–683. doi:10.1038/nsmb.1455.

Diaz, E., G. Ayala, M.E. Diaz, Liang-Wei Gong, and D. Toomre. 2010. Automatic Detection of Large Dense-Core Vesicles in Secretory Cells and Statistical Analysis of Their Intracellular Distribution. *IEEE/ACM Trans. Comput. Biol. Bioinforma.* 7:2–11. doi:10.1109/TCBB.2008.30.

Elhamdani, A., F. Azizi, and C.R. Artalejo. 2006. Double patch clamp reveals that transient fusion (kiss-and-run) is a major mechanism of secretion in calf adrenal chromaffin cells: High calcium shifts the mechanism from kiss-and-run to complete fusion. *J. Neurosci.* 26:3030–3036. doi:10.1523/JNEUROSCI.5275-05.2006.

Engle, E.C. 2010. Human Genetic Disorders of Axon Guidance. *Cold Spring Harb. Perspect. Biol.* 2:a001784–a001784. doi:10.1101/cshperspect.a001784.

Fuschini, G., T. Cotrufo, O. Ros, A. Muhaisen, R. Andrés, J.X. Comella, and E. Soriano. 2018. Syntaxin-1/TI-VAMP SNAREs interact with Trk receptors and are required for neurotrophin-dependent outgrowth. *Oncotarget*. 9:35922–35940. doi:10.18632/oncotarget.26307.

Galli, T., A. Zahraoui, V. V. Vaidyanathan, G. Raposo, J.M. Tian, M. Karin, H. Niemann, and D. Louvard. 1998. A Novel Tetanus Neurotoxin-insensitive Vesicle-associated Membrane Protein in SNARE Complexes of the Apical Plasma Membrane of Epithelial Cells. *Mol. Biol. Cell*. 9:1437–1448. doi:10.1091/mbc.9.6.1437.

Gauthier, N.C., M.A. Fardin, P. Roca-Cusachs, and M.P. Sheetz. 2011. Temporary increase in plasma membrane tension coordinates the activation of exocytosis and contraction during cell spreading. *Proc. Natl. Acad. Sci.* 108:14467–14472. doi:10.1073/pnas.1105845108.

Grantham, N. 2012. Analyzing multiple independent spatial point processes. 1–41.

Guček, A., J. Jorgačevski, P. Singh, C. Geisler, M. Lisjak, N. Vardjan, M. Kreft, A. Egner, and R. Zorec. 2016. Dominant negative SNARE peptides stabilize the fusion pore in a narrow,

release-unproductive state. *Cell. Mol. Life Sci.* 73:3719–3731. doi:10.1007/s00018-016-2213-2.

Hayashi, T., H. McMahon, S. Yamasaki, T. Binz, Y. Hata, T.C. Südhof, and H. Niemann. 1994. Synaptic vesicle membrane fusion complex: action of clostridial neurotoxins on assembly. *EMBO J.* 13:5051–61.

He, L., and L.-G. Wu. 2007. The debate on the kiss-and-run fusion at synapses. *Trends Neurosci.* 30:447–455. doi:10.1016/j.tins.2007.06.012.

Holroyd, P., T. Lang, D. Wenzel, P. De Camilli, and R. Jahn. 2002. Imaging direct, dynamin-dependent recapture of fusing secretory granules on plasma membrane lawns from PC12 cells. *Proc. Natl. Acad. Sci.* 99:16806–16811. doi:10.1073/pnas.222677399.

Holt, M., F. Varoqueaux, K. Wiederhold, S. Takamori, H. Urlaub, D. Fasshauer, and R. Jahn. 2006. Identification of SNAP-47, a Novel Qbc-SNARE with Ubiquitous Expression. *J. Biol. Chem.* 281:17076–17083. doi:10.1074/jbc.M513838200.

Hua, Z., S. Leal-Ortiz, S.M. Foss, C.L. Waites, C.C. Garner, S.M. Voglmaier, and R.H. Edwards. 2011. v-SNARE Composition Distinguishes Synaptic Vesicle Pools. *Neuron*. 71:474–487. doi:10.1016/j.neuron.2011.06.010.

Karatekin, E. 2018. Toward a unified picture of the exocytotic fusion pore. *FEBS Lett.* 592:3563–3585. doi:10.1002/1873-3468.13270.

Link, E., L. Edelmann, J.H. Chou, T. Binz, S. Yamasaki, U. Eisel, M. Baumert, T.C. Südhof, H. Niemann, and R. Jahn. 1992. Tetanus toxin action: Inhibition of neurotransmitter release linked to synaptobrevin proteolysis. *Biochem. Biophys. Res. Commun.* 189:1017–1023. doi:10.1016/0006-291X(92)92305-H.

Logan, T., J. Bendor, C. Toupin, K. Thorn, and R.H. Edwards. 2017. α-Synuclein promotes dilation of the exocytotic fusion pore. *Nat. Neurosci.* 20:681–689. doi:10.1038/nn.4529.

Miesenböck, G., D.A. De Angelis, and J.E. Rothman. 1998. Visualizing secretion and synaptic transmission with pH-sensitive green fluorescent proteins. *Nature*. 394:192–195. doi:10.1038/28190.

Napolitano, L.M., and G. Meroni. 2012. TRIM family: Pleiotropy and diversification through homomultimer and heteromultimer formation. *IUBMB Life*. 64:64–71. doi:10.1002/iub.580.

Paul, L.K., W.S. Brown, R. Adolphs, J.M. Tyszka, L.J. Richards, P. Mukherjee, and E.H. Sherr. 2007. Agenesis of the corpus callosum: genetic, developmental and functional aspects of connectivity. *Nat. Rev. Neurosci.* 8:287–299. doi:10.1038/nrn2107.

Pelleg, D., D. Pelleg, and A. Moore. 2000. X-means: Extending K-means with Efficient Estimation of the Number of Clusters. *Proc. 17TH Int. CONF. Mach. Learn.* 727--734.

Pfenninger, K.H. 2009. Plasma membrane expansion: a neuron's Herculean task. *Nat. Rev. Neurosci.* 10:251–61. doi:10.1038/nrn2593.

Rizzoli, S.O., and R. Jahn. 2007. Kiss-and-run, Collapse and 'Readily Retrievable' Vesicles. *Traffic*. 8:1137–1144. doi:10.1111/j.1600-0854.2007.00614.x.

Rousseeuw, P.J. 1987. Silhouettes: A graphical aid to the interpretation and validation of cluster analysis. *J. Comput. Appl. Math.* 20:53–65. doi:10.1016/0377-0427(87)90125-7.

Roux, K.J., D.I. Kim, M. Raida, and B. Burke. 2012. A promiscuous biotin ligase fusion protein identifies proximal and interacting proteins in mammalian cells. *J. Cell Biol.* 196:801–810. doi:10.1083/jcb.201112098.

Schoch, S. 2001. SNARE Function Analyzed in Synaptobrevin/VAMP Knockout Mice. *Science (80-.).* 294:1117–1122. doi:10.1126/science.1064335.

Segovia, M., E. Ales, M.A. Montes, I. Bonifas, I. Jemal, M. Lindau, A. Maximov, T.C. Sudhof, and G. Alvarez de Toledo. 2010. Push-and-pull regulation of the fusion pore by synaptotagmin-7. *Proc. Natl. Acad. Sci.* 107:19032–19037. doi:10.1073/pnas.1014070107.

Shimojo, M., J. Courchet, S. Pieraut, N. Torabi-Rander, R. Sando Iii, F. Polleux, A. Maximov, R. Sando, F. Polleux, A. Maximov, and A. Maximov. 2015. No Title. *Cell Rep.* 11:1054–66. doi:10.1016/j.celrep.2015.04.032.

Short, K.M., and T.C. Cox. 2006. Subclassification of the RBCC/TRIM Superfamily Reveals a Novel Motif Necessary for Microtubule Binding. *J. Biol. Chem.* 281:8970–8980. doi:10.1074/jbc.M512755200.

Söllner, T., S.W. Whiteheart, M. Brunner, H. Erdjument-Bromage, S. Geromanos, P. Tempst, and J.E. Rothman. 1993. SNAP receptors implicated in vesicle targeting and fusion. *Nature*. 362:318–324. doi:10.1038/362318a0.

Staykova, M., D.P. Holmes, C. Read, and H.A. Stone. 2011. Mechanics of surface area regulation in cells examined with confined lipid membranes. *Proc. Natl. Acad. Sci.* 108:9084–9088. doi:10.1073/pnas.1102358108.

Sudhof, T.C., and J.E. Rothman. 2009. Membrane Fusion: Grappling with SNARE and SM Proteins. *Science (80-.).* 323:474–477. doi:10.1126/science.1161748.

Sugar, C.A., and G.M. James. 2003. Finding the Number of Clusters in a Dataset. *J. Am. Stat. Assoc.* 98:750–763. doi:10.1198/016214503000000666.

Urbina, F.L., S.M. Gomez, and S.L. Gupton. 2018a. Spatiotemporal organization of exocytosis emerges during neuronal shape change. *J. Cell Biol.* 217:1113–1128. doi:10.1083/jcb.201709064.

Viesselmann, C., J. Ballweg, D. Lumbard, and E.W. Dent. 2011. Nucleofection and primary culture of embryonic mouse hippocampal and cortical neurons. *J. Vis. Exp.* doi:10.3791/2373.

Wang, C.-T., J.-C. Lu, J. Bai, P.Y. Chang, T.F.J.J. Martin, E.R. Chapman, and M.B. Jackson. 2003. Different domains of synaptotagmin control the choice between kiss-and-run and full fusion. *Nature*. 424:943–947. doi:10.1038/nature01857.

Wen, P.J., S. Grenklo, G. Arpino, X. Tan, H.-S. Liao, J. Heureaux, S.-Y. Peng, H.-C. Chiang, E. Hamid, W.-D. Zhao, W. Shin, T. Näreoja, E. Evergren, Y. Jin, R. Karlsson, S.N. Ebert, A. Jin, A.P. Liu, O. Shupliakov, and L.-G. Wu. 2016. Actin dynamics provides membrane tension to merge fusing vesicles into the plasma membrane. *Nat. Commun.* 7:12604. doi:10.1038/ncomms12604.

Winkle, C.C., L.M. McClain, J.G. Valtschanoff, C.S. Park, C. Maglione, and S.L. Gupton. 2014. A novel Netrin-1–sensitive mechanism promotes local SNARE-mediated exocytosis during axon branching. *J. Cell Biol.* 205:217–232. doi:10.1083/jcb.201311003.

Winkle, C.C., R.H.J. Olsen, H. Kim, S.S. Moy, J. Song, and S.L. Gupton. 2016. Trim9 Deletion Alters the Morphogenesis of Developing and Adult-Born Hippocampal Neurons and Impairs Spatial Learning and Memory. *J. Neurosci.* 36:4940–4958. doi:10.1523/JNEUROSCI.3876-15.2016.

Yuan, T., J. Lu, J. Zhang, Y. Zhang, and L. Chen. 2015. Spatiotemporal Detection and Analysis of Exocytosis Reveal Fusion “Hotspots” Organized by the Cytoskeleton in Endocrine Cells. *Biophys. J.* 108:251–260. doi:10.1016/j.bpj.2014.11.3462.